Extension of the virtual fields method to elasto-plastic material identification with cyclic loads and kinematic hardening

Fabrice Pierron, Stéphane Avril, Vinh The Tran

Extension of the virtual fields method to elasto-plastic material identification with cyclic loads and kinematic hardening

F. Pierron[a], S. Avril[b] and V. The Tran[a]

[a] *Laboratoire de Mécanique et Procédés de Fabrication, Arts et Metiers ParisTech, Rue Saint-Dominique, BP 508, 51006 Châlons-en-Champagne Cedex, France*

[b] *Center for Health Engineering, Ecole Nationale Supérieure des Mines de St-Etienne, 158 cours Fauriel, 42023 Saint-Etienne, France.*

vinh.tran@chalons.ensam.fr ; avril@emse.fr ; fabrice.pierron@ensam.eu

Abstract

The virtual fields method (VFM) has been specifically developed for solving inverse problems from dense full-field data. This paper explores recent improvements regarding the identification of elasto-plastic models. The procedure has been extended to cyclic loads and combined kinematic/isotropic hardening. A specific attention has also been given to the effect of noise in the data. Indeed, noise in experimental data may significantly affect the robustness of the VFM for solving such inverse problems. The concept of optimized virtual fields that minimize the noise effects, previously developed for linear elasticity, is extended to plasticity in this study. Numerical examples with models combining isotropic and kinematic hardening have been considered for the validation. Different load paths (tension, compression, notched specimen) have shown that this new procedure is robust when applied to elasto-plastic material identification. Finally, the procedure is validated on experimental data.

Key words: virtual fields method, optimized virtual fields, full-field measurement, elasto-plastic behaviour, isotropic hardening, kinematic hardening, heterogeneous tests, cyclic loading, inverse problem.

LIST OF NOTATIONS AND SYMBOLS

Global variables:

$\underline{\underline{\sigma}}$: stress tensor,

$\underline{\underline{\varepsilon}}^{\star}$: virtual strain tensor,

$\boldsymbol{\sigma}$: stress vector (plane stress),

$\boldsymbol{\epsilon}$: strain vector (plane stress),

$\boldsymbol{u}^{\star}$: virtual displacement vector,

$\boldsymbol{T}$: vector of tractions on the boundary,

V: volume of the specimen,

b: thickness of the specimen,

dS: infinitesimal area,

$[M_{X_P}(x, y, t)]$: tangent stiffness matrix,

x, y : space variable,

X_P: constitutive parameters,

t: time,

$W^{*}_{ext}(t_n)$: virtual work of the external forces from the beginning of the test up to time t_n,

$F(t_n)$: resultant load at these given times.

Elementary variables:

A : area of the specimen (area of interest),

A_i^{el} : area of a given finite element of index i,

$\{\dot{U}_i^{el}(t)\}$: time derivative of the vector of actual nodal displacements at the nodes of element i,

$\{\delta\dot{U}_i^{el}(t)\}$: error (due to experimental noise) in the vector of nodal displacement time derivatives of a given finite element of index i,

$[B_i^{el}(t_n)] = [B_i^{el}]$: gradient matrix of a given finite element of index i,

$[K_i^{el}(X_P, t)]$: stiffness matrix of a given finite element of index i,

$[K]$: assembled stiffness matrix,

x_i: abscissa of the centre of a given finite element of index i,

y_i: ordinate of the centre of a given finite element of index i,

$\Phi(X_P)$: total cost function,

Ψ_n: cost function for virtual fields selection,

J_n: components of the cost function (deviation from the principle of virtual work at time t_n),

$E(.)$: expectation of a random distribution,

$V(.)$: variance of a random distribution.

Numbering:

P : number of constitutive parameters,

k: index referring to constitutive parameters ($1 \leq k \leq P$),

N: number of load steps,

n: index referring to load steps ($1 \leq n \leq N$),

I: number of finite elements,

i: index referring to finite elements ($1 \leq i \leq I$).

Operators:

$\underline{\underline{a}} \bigotimes \underline{\underline{b}}$: tensorial product between tensors $\underline{\underline{a}}$ and $\underline{\underline{b}}$,

$\underline{\underline{a}} : \underline{\underline{b}}$: contracted product between tensors $\underline{\underline{a}}$ and $\underline{\underline{b}}$,

$\boldsymbol{a} \cdot \boldsymbol{b}$: scalar product between vectors $\boldsymbol{a}$ and $\boldsymbol{b}$,

$\{\}^T$ or $[]^T$: denotes the transpose of a vector or a matrix.

1. Introduction

The use of full-field measurements is gradually changing the experimental approaches to the identification of constitutive equations of materials. Indeed, having access to a great number of kinematic data points at the surface of a specimen enables to perform more complex tests that bear more information on the material behaviour. However, the data reduction is more complex and often has to resort to some sort of inverse solution. There are different strategies to solve this problem, as reported in [1].

Several attempts at solving this type of problem for elasto-plastic behaviour can be found in the literature [2, 3, 4, 5, 6, 7], using finite element model updating. The idea is to build up a finite element model of the test to be performed using initial input values for the parameters to be retrieved. Then, the experimental data (displacements, strains and/or forces) are compared to the computed ones through a cost function to be minimized. Obviously, issues concerning existence and uniqueness of the solution are of primary importance here and depend greatly on the choice of the test, the amount of measured data and the quality of the cost function, as discussed for instance by [8]. Computation time is also a critical issue. An alternative is the virtual fields method (VFM) with the advantage of requiring much less computation time [9, 10, 11]. Other important features are the fact that no finite element analysis is required and that the procedure is insensitive to to the distribution of the external loading if suitable virtual fields are used.

In a previous study, an experimental validation of the use of the VFM to identify the parameters of an elasto-plastic constitutive model (Voce's non-linear hardening model) was presented [10]. A tensile test was carried out on a plane dog-bone specimen. Although not statically determined, this test provided very simple stress and strain distributions because in first approximation, the longitudinal stress only varied as a function of the longitudinal axis of the specimen and the other stress components remained small. The curve of the identified model was in very good agreement with the ones obtained on standard uniform stress tests using strain gauges data [10]. However, this configuration was only a first attempt on a simplistic case since only one stress component was considered and loading was proportional because of the simple shape of the specimen.

In another study, an experimental validation with more complex geometries that make

all the in-plane components of the stress tensor contribute was considered [11]. Six mild steel double-notched specimens were tested in a configuration combining tension and in-plane bending. The identified parameters were in good agreement with their reference counterparts. This study showed that it is possible to identify elasto-plastic parameters from tests giving rise to heterogeneous stress fields and to complex yield flows. Stress fields were derived directly from the measured data and updated until the principle of virtual work was satisfied. Nevertheless, the experimental results were obtained for quite simple elasto-plastic constitutive equations (only four or five parameters) and simple virtual fields were used. No specific rule was considered for this choice, though an infinite number of possible virtual fields exists. Intensive work has been devoted recently to the choice of optimal virtual fields in the case of anisotropic elasticity [12, 13], but the obtained results could not be applied to elasto-plasticity because of the non-linear nature of the constitutive equations in this case. This paper presents a solution to the issue of virtual field selection in elasto-plasticity, along with an extension of the VFM to combined isotropic and kinematic hardening laws. Different load cases (tension, unloading, compression, unloading) are considered. The identification procedure of the elasto-plastic constitutive parameters is based on that presented in [11] with the following improvements:

- the stress rate is derived directly from the measured total strain rate by using a tangent matrix,
- optimal virtual fields are devised by using the tangent matrix for assessing the sensitivity to noise of the method,
- a dedicated algorithm is used for the minimization of the cost function, thus reducing computation time,
- combined isotropic and kinematic hardening can be handled,
- loading cycles instead of monotonic loading are considered.

To the best knowledge of the present authors, it is the first time that inverse identification from full-field measurements is performed in elasto-plasticity on cyclic loadings and also the first time that combined isotropic and kinematic hardening is considered. The other originality of the paper is clearly the selection of optimized virtual fields in elasto-plasticity.

After a description of these improvements, this paper validates the approach with simulated data and the performances with regard to noise handling are reported. Then, an experimental validation is presented.

2. Identification procedure

2.1. General principle

The procedure for extracting the constitutive parameters uses the virtual fields method (VFM). The VFM is based on the principle of virtual work. This principle can be written as follows for a given solid of volume V subjected to a quasi static loading in absence of body forces:

$$-\int_V \underline{\underline{\sigma}} : \underline{\underline{\varepsilon}}^\star dV + \int_{\partial V_f} \boldsymbol{T}.\boldsymbol{u}^\star dS = 0 \tag{1}$$

where $\underline{\underline{\sigma}}$ is the actual stress tensor, $\underline{\underline{\varepsilon}}^\star$ is the virtual strain tensor, $\boldsymbol{T}$ is the vector of loading tractions acting on the boundary, ∂V_f is the part of the solid boundary where the tractions are applied and $\boldsymbol{u}^\star$ is the virtual displacement field vector. A virtual displacement field is actually a test function, defined across volume V, for which the previous equation is verified, and the virtual strain tensor is the strain tensor derived from the given virtual displacement. An important feature is the fact that $\boldsymbol{u}^\star$ must be kinematically admissible. It means that $\boldsymbol{u}^\star$ must be continuous and differentiable across the whole volume and it must be null or constant over boundaries where the reaction traction distributions are unknown, in order to involve only the measured resultant loads in the equations.

In this study, the specimens which were considered have a constant thickness, denoted b, which is small compared to the other dimensions. Only in-plane loading is considered. Hence, a state of plane stress is assumed and tensors $\underline{\underline{\sigma}}$ and $\underline{\underline{\varepsilon}}$ are turned into vectors $\boldsymbol{\sigma}$ and $\boldsymbol{\epsilon}$ according to the following convention:

$$\boldsymbol{\sigma} = \left\{ \begin{array}{c} \sigma_{xx} \\ \sigma_{yy} \\ \sigma_{xy} \end{array} \right\} \quad \text{and} \quad \boldsymbol{\epsilon} = \left\{ \begin{array}{c} \epsilon_{xx} \\ \epsilon_{yy} \\ 2\epsilon_{xy} \end{array} \right\} \tag{2}$$

Both $\boldsymbol{\sigma}$ and $\boldsymbol{\epsilon}$ are functions of three variables: time t and space variables x and y. Quantities $\boldsymbol{\epsilon}(x, y, t)$ are derived from the measured displacement fields, denoted $\boldsymbol{u}(x, y, t)$, by spatial differentiation with respect to x and y (see details in Appendix A):

$$\boldsymbol{\epsilon} = \left\{ \begin{array}{c} \epsilon_{xx} \\ \epsilon_{yy} \\ 2\epsilon_{xy} \end{array} \right\} = \left\{ \begin{array}{c} \dfrac{\partial u_x}{\partial x} \\ \dfrac{\partial u_y}{\partial y} \\ \dfrac{\partial u_x}{\partial y} + \dfrac{\partial u_y}{\partial x} \end{array} \right\} \tag{3}$$

The infinitesimal formulation of the strain tensor is used in this work because the strains remain lower than 8%. However, for a possible further use of the procedure with higher strains, the Green-Lagrange tensor may be used instead [14], as $\boldsymbol{u}(x, y, t)$ is provided in the initial configuration. An application of the VFM in large deformations can be found in [15, 16].

The constitutive equations have now to be introduced to derive $\boldsymbol{\sigma}(x, y, t)$. In order to include both elasticity and plasticity in a general framework, the stress rate $\dot{\boldsymbol{\sigma}} = d\boldsymbol{\sigma}/dt$ may be written like this:

$$\dot{\boldsymbol{\sigma}}(x, y, t) = [M_{X_P}(x, y, t)]\dot{\boldsymbol{\epsilon}}(x, y, t) \tag{4}$$

where $[M_{X_P}(x, y, t)]$ is the stiffness matrix in elasticity or a mere tangent matrix in plasticity. The latter varies with time and location because it depends on the actual strain rate $\dot{\boldsymbol{\epsilon}} = d\boldsymbol{\epsilon}/dt$ and on the actual stress rate $\dot{\boldsymbol{\sigma}}(x, y, t)$. The evolution of $[M_{X_P}(x, y, t)]$ is driven by the constitutive equations of the materials. In this study, it is assumed that the constitutive equations are parameterized by a given number of material properties (denoted X_P) which are called the constitutive parameters. These parameters are unknown as the aim of this study is to propose an approach to their identification. The constitutive parameters are denoted X_P, $1 \leq k \leq P$, where P is the number of unknown constitutive parameters (see details in Appendix B). Assuming that the initial strain is zero, Eq. 1 may be rewritten as:

$$-\int_A \boldsymbol{\epsilon}^*(x, y, t_n) \cdot \left\{ \int_0^{t_n} [M_X(x, y, t)]\dot{\boldsymbol{\epsilon}}(x, y, t)\ dt \right\} dxdy + \frac{1}{b} W^*_{ext}(t_n) = 0 \tag{5}$$

where A is the measurement area, b the thickness of the specimen, $[M_{X_P}(x, y, t)]$ the tangent matrix relating stress rate to strain rate (it is the stiffness matrix if the strains are elastic and it

depends on the stresses during plasticity) and $W^*_{ext}(t_n)$ is the virtual work of the external forces provided from the beginning of the test up to time t_n.

2.2. Data processing

In practice, displacement data will be measured at discrete locations across the surface of the specimen thanks to optical methods like the grid method [10, 11] or Digital Image Correlation (DIC) [17, 18, 19]. Generally, the discrete locations where data are available define a grid onto the region of interest of the specimen. If data are independently measured from one grid point to another, the period of the grid defines the spatial resolution of the measurement technique.

No displacement data can be measured between these grid points. In order to deduce the whole displacement field everywhere across the region of interest, and also for filtering the noise contained in the data, a global reconstruction procedure may be used in practice. Least-squares approximation is a relevant tool for achieving this reconstruction [12]. A basis of shape functions is used to define the approximate reconstructed fields, and the coefficients of each shape function in the basis are computed by fitting in the least-squares sense the data measured at the grid points. In practice, the most commonplace basis of shape functions is a basis of piecewise linear functions defined over triangular elements in the region of interest. As the objective here is to investigate the global identification process from the raw data to obtain constitutive parameters, the reconstruction process will be included in the following equations of the VFM. Moreover, for the sake of simplicity in the computations, it was shown [12] that the same piecewise linear functions defined from a triangular mesh can be used for defining continuous virtual fields. It should be noted that only the virtual displacements have to be continuous, not the virtual strains. The total number of triangles used to define the basis of piecewise linear functions is denoted m. More details about the piecewise linear functions are given in Appendix A.

The measurements are usually performed at different times evenly distributed all along the test, before and after the onset of plasticity. These times are denoted t_n and the tensile resultant load, denoted $F(t_n)$, is also measured at these given times. The number of measurement times is denoted N. Then, one can calculate $W^*_{ext}(t_n)$ as the virtual work of the resultant load, measured classically in experiments thanks to a load cell.

According to the previous comments and according to the form of shape functions used in this approach (Appendix A), Eq. 5 may be rewritten as follows at time t_n:

$$\sum_{i=1}^{I} A_i^{el} \{U_i^{*el}(t_n)\}^T [B_i^{el}]^T \left\{ \int_0^{t_n} [M_{X_P}(x_i, y_i, t)][B_i^{el}] \{\dot{U}_i^{el}(t)\} dt \right\} = \frac{1}{b} W_{ext}^*(t_n)$$

leading to:

$$\sum_{i=1}^{I} \int_0^{t_n} \{U_i^{*el}(t_n)\}^T \underbrace{A_i^{el} [B_i^{el}]^T [M_{X_P}(x_i, y_i, t)][B_i^{el}]}_{[K_i^{el}(X_P, t)]} \{\dot{U}_i^{el}(t)\} dt = \frac{1}{b} W_{ext}^*(t_n) \tag{6}$$

where $\{U_i^{*el}(t_n)\}$ is the vector of virtual nodal displacements at the nodes of element i and at time t_n, $\{\dot{U}_i^{el}(t)\}$ is the derivative with respect to time of the vector of actual nodal displacements at the nodes of element i (actual nodal velocities), I is the total number of triangles, $[B_i^{el}]$ is a matrix containing the gradients of the shape functions of the triangular linear element used here and $[M_{X_P}(x_i, y_i, t)]$ is the tangent matrix of element i at time t (evaluated at the centre of gravity of each element) and A_i^{el} is the area of element i. As is usual in finite element calculations, the elementary tangent stiffness matrix $[K_i^{el}(X_P, t)]$ is defined as shown with the bracket in Eq. 6 (it is only known implicitly because it depends on the stresses at time t and on the constitutive parameters to be identified).

2.3. Inverse problem resolution

In a forward problem, the unknown in Eq. 6 would be $\{\dot{U}_i^{el}(t)\}$ for all the elements i. In an inverse problem, which is the currently considered problem, the unknown in Eq. 6 is the tangent stiffness matrix at each time t, denoted $[K_i^{el}(X_P, t)]$. Actually, the number of unknowns is not as large as the number of components in $[K_i^{el}(X_P, t)]$. Indeed, $[K_i^{el}(X_P, t)]$ implicitly depends on the constitutive parameters to be identified: X_P. If the X_P parameters were known, $[K_i^{el}(X_P, t)]$ would be known entirely for all the elements i. Therefore, at a given time t_n and for a given virtual field $\{U^*(t_n)\}$, only the X_P parameters are unknown in Eq. 6. Consequently, the resolution of the inverse problem can be achieved by solving Eq. 6 for a given virtual field $\{U^*(t_n)\}$. One of the key aspects of this resolution is the choice of relevant virtual fields $\{U^*(t_n)\}$. Usually, it is necessary to use different virtual fields and to build up a system of equations where the equations are sufficiently independent to involve all the unknown parameters. The choice of the virtual fields will be discussed in Section 3. Two cases must be distinguished.

- Identification of the elastic parameters: the constitutive equations depend linearly on the constitutive parameters. In this case, writing Eq. 6 with as many virtual fields as unknowns leads to a linear system which directly provides the parameters after inversion, if they contribute sufficiently to the response and if the virtual fields are independent [11, 12]. In this paper, the identification procedure of the elastic parameters is not investigated. The method presented in [10] using optimal virtual fields provides good results and will be employed here.

- Identification of the plastic parameters: the constitutive equations are not linear functions of the constitutive parameters. The identification strategy relies in this case on the minimization of a residual constructed with Eq. 6. The cost function that one has to minimize here is built up so that n equations may be derived from Eq. 6.

$$\Phi(X_P) = \sum_{n=1}^{N} \left[- \sum_{i=1}^{I} \int_0^{t_n} \{U_i^{*el}(t_n)\}^T [K_i^{el}(X_P, t)] \{\dot{U}_i^{el}(t)\} dt + \frac{1}{b} W_{ext}^*(t_n) \right]^2 \tag{7}$$

Obviously $\Phi(X_P)$ will be zero for the actual parameters and for any kinematically admissible virtual field $\{U^*(t_n)\}$ if the actual displacements are known without uncertainty. Hence the identification method is carried out by minimizing the above cost function $\Phi(X_P)$ with respect to the constitutive parameters X_P. In other words, the actual parameters are those which lead to the best fit of the equilibrium written with the principle of virtual work. Since $\Phi(X_P)$ can be calculated for any trial value of the constitutive parameters, one can choose a random starting point and minimize $\Phi(X_P)$ from this point.

2.4. Application to elasto-plasticity

The VFM has already been applied to elasto-plasticity. Compared to previously published material [9, 10, 11], the originality of this study is to consider more sophisticated constitutive equations and cyclic loading and to investigate the optimization of the selection of the virtual fields.

The constitutive model considered in this study combines isotropic and kinematic hardening laws. Two cases for matrix $[M_{X_P}(x, y, t)]$ in Eq. 4 must be distinguished.

First, before the elastic limit, $[M_{X_P}(x,y,t)]$ is the stiffness matrix, usually denoted Q in plane stress. Linear isotropic elasticity is considered:

$$[Q] = \begin{bmatrix} X_1 & X_2 & 0 \\ X_2 & X_1 & 0 \\ 0 & 0 & \dfrac{(X_1 - X_2)}{2} \end{bmatrix} \tag{8}$$

where $X_1 = \frac{E}{1-\nu^2}$; $\quad X_2 = \frac{\nu E}{1-\nu^2}$, E is Young's modulus, ν Poisson's ratio.

Secondly, beyond the elastic limit, $[M_{X_P}(x,y,t)]$ is the tangent stiffness matrix in plasticity. Assuming a yield criterion (Von Mises), a flow rule (associated plasticity) and a hardening law (combined isotropic and kinematic), it is possible to express the stress rate $\dot{\boldsymbol{\sigma}}(x,y,t)$ as a function of the measured total strain rate $\dot{\boldsymbol{\epsilon}}(x,y,t)$ (details are provided in Appendix B). One obtains:

$$\begin{Bmatrix} \dot{\sigma}_{xx} \\ \dot{\sigma}_{yy} \\ \dot{\sigma}_{xy} \end{Bmatrix} = \underbrace{\left[[Q]^{-1} + \frac{\boldsymbol{S} \bigotimes \boldsymbol{S}}{\left(\frac{3}{2}C - \gamma \boldsymbol{S1} \cdot \boldsymbol{X}\right) + H} \right]^{-1}}_{\text{tangent stiffness matrix } [M]} \begin{Bmatrix} \dot{\varepsilon}_{xx} \\ \dot{\varepsilon}_{yy} \\ 2\dot{\varepsilon}_{xy} \end{Bmatrix} \tag{9}$$

where $\boldsymbol{S} = \begin{Bmatrix} \frac{\partial f}{\partial \sigma_{xx}} \\ \frac{\partial f}{\partial \sigma_{yy}} \\ 2\frac{\partial f}{\partial \sigma_{xy}} \end{Bmatrix}$ is a column vector deduced from the stress deviator, $\boldsymbol{S1} = \begin{Bmatrix} \frac{\partial f}{\partial X_{xx}} \\ \frac{\partial f}{\partial X_{yy}} \\ 2\frac{\partial f}{\partial X_{xy}} \\ \frac{\partial f}{\partial X_{zz}} \end{Bmatrix}$ is a column vector deduced from the yield surface translation vector $\boldsymbol{X}$, f is the yield criterion, C and γ are kinematic hardening parameters, $\sigma_s(p)$ is the current yield stress of the material which is a function of the hardening parameters, p the cumulated equivalent plastic strain and $[Q]$ the elastic stiffness matrix.

3. Selection of the virtual fields

3.1. General rules

As shown in Eq. 7, virtual fields must be chosen and input in the principle of virtual work to write up the global equilibrium of the specimen. Extensive work has been devoted

recently to the choice of optimal virtual fields in the case of anisotropic elasticity [12, 13], but this procedure could not be applied directly in elasto-plasticity because of the non-linear nature of the constitutive equations in this case. Nevertheless, one can use the same principles as that presented in [13]. The idea is to estimate the effect of noisy data onto the identification and to use the virtual fields that minimize these effects.

3.2. Effect of noisy data on the cost function

Because of experimental noise, the measured values of the displacements are different from the actual ones which can be written as:

$$\{\dot{U}_i^{el}(t)\} = \{\widetilde{\dot{U}_i^{el}}(t)\} + \{\delta\dot{U}_i^{el}(t)\} \tag{10}$$

where $\{\dot{U}_i^{el}(t)\}$ is the exact value of the displacement rate, $\{\widetilde{\dot{U}_i^{el}}(t)\}$ the measured displacement rate and $\{\delta\dot{U}_i^{el}(t)\}$ is the error on the measured displacement rate coming from experimental noise. Accordingly, the error in Eq. 6 is given by:

$$\begin{aligned}
\delta J_n &= \sum_{i=1}^{I} \int_0^{t_n} \{U_i^{*el}(t_n)\}^T [K_i^{el}(X_P,t)] \{\delta\dot{U}_i^{el}(t)\}\, dt \\
&= \sum_{i=1}^{I} \sum_{j=1}^{n} \underbrace{\{U_i^{*el}(t_n)\}^T [K_i^{el}(X_P,t_j)]}_{\{g_{ij}\}} \underbrace{\{\delta\dot{U}_i^{el}(t_j)\Delta t\}}_{\{f_{ij}\}} \\
&= \sum_{j=1}^{n} \underbrace{\{U^*(t_n)\}^T [K(X_P,t_j)]}_{\{g_j\}} \underbrace{\{\delta\dot{U}(t_j)\Delta t\}}_{\{f_j\}}
\end{aligned} \tag{11}$$

The time integration $\int_0^{t_n}$ has been changed into a discrete sum with an explicit Euler integration scheme. The time step for the integration is denoted Δt. Experimentally, Δt is the time step separating two consecutive measurements. It is constant throughout the tests.

One can estimate the effect of noisy data from Eq. 11. Indeed, the error contains three distinct quantities.

1. The first one $\{U^*(t_n)\}^T$ comes from the choice of the virtual field.

2. The second one $[K(X_P, t_j)]$ is the tangent stiffness matrix, which depends on the unknown properties of the material, on the geometry of the specimen, but also on the loading history. As $[K(X_P, t_j)]$ involves the loading history, it is computed from the measured deformation data, and therefore it depends on $\{\dot{U}_i^{el}(t_k)\}$ for k varying from 1 to $j-1$. The consequence of this is that $[K(X_P, t_j)]$ is not a deterministic matrix but it has a random part depending on the data noise of the different time steps from t_1 up to t_{j-1}.
3. The third one is the random part of the measured deformation data, assumed to be pure white noise here.

Eq. 11 shows that the only term that can be controlled in the error is the virtual field. The objective of this paper is to choose the virtual fields that minimize the effects of the white noise in order to obtain the most robust possible results.

To study the effect of the white noise present in the data, it is important to define precisely the statistical properties of this white noise. Representing white noise, vectors $\{f_j\}$ in Eq. 11 have a null expectation: $E(\{f_j\}) = \{0\}$ and their covariance matrix is diagonal such that $Cov(\{f_j\}) = \gamma_u^2[D]$, where $[D]$ is the identity matrix and γ_u is a scalar equal to the resolution of the measurement method.

However, an important property to be noticed is that $\{f_k\}$ and $\{f_{k-1}\}$ are correlated. Indeed, the measurement of deformation at time t_k involves an image of the specimen at times t_k and t_{k-1} whereas the measurement of deformation at time t_{k-1} involves an image of the specimen at times t_{k-1} and t_{k-2}. This proves that the measurement of deformation at time t_k and at time t_{k-1} involves a common image, hence $\{\delta\dot{U}_i^{el}(t_k)\}$ and $\{\delta\dot{U}_i^{el}(t_{k-1})\}$ are correlated. This has two consequences:

1. the first one is that the expectation of $\{f_j\}$ times $\{f_{j-1}\}$ is not null,
2. the second one is that the expectation of $\{f_j\}$ times $\{g_j\}$ is not null either as $\{g_j\}$ is computed from the previous deformation fields, so it also depends on $\{f_{j-1}\}$.

Therefore, the white noise has two effects on the cost function:

- a systematic bias because the expectation of δJ_n involves the expectation of g_j times f_j. The bias in the cost function is further denoted $E(\delta J_n)$,

- random variations or scattering which can be characterized by the variance of δJ_n, further denoted $V(\delta J_n)$.

To determine the optimal choice of virtual fields, one will study the variance of the random error due to the white noise.

The variance of δJ_n can then be written as:

$$\begin{aligned}
V(\delta J_n) &= E([\delta J_n - E(\delta J_n)]^2) = E({\delta J_n}^2) + [E(\delta J_n)]^2 \\
&= E\left(\left[\sum_{j=1}^{n} g_j f_j\right]^2\right) + [E(\delta J_n)]^2 \\
&= \left(\sum_{j=1}^{n} E\left(g_j^2 f_j^2\right) + 2\sum_{j=1}^{n}\sum_{k(\neq j)}^{n} E(g_j g_k f_j f_k)\right) + [E(\delta J_n)]^2 \\
&= \gamma_u^2 \sum_{j=1}^{n} g_j^2 + 2\sum_{j=2}^{n} E(g_j g_{j-1} f_j f_{j-1}) + [E(\delta J_n)]^2 \\
&= \gamma_u^2 \sum_{j=1}^{n} \{U^*(t_n)\}^T [K(X_P, t_j)][K(X_P, t_j)]\{U^*(t_n)\} + \mathfrak{B} \\
&= \gamma_u^2 \Psi_n + \mathfrak{B}
\end{aligned} \tag{12}$$

where $\mathfrak{B}$ denote the terms involving biases that come from the correlation between $\{f_j\}$ and $\{f_{j-1}\}$, and Ψ_n is a deterministic factor that scales the noise influence and depends only on the choice of the virtual field, the geometry and the mechanical properties of material.

3.3. Determination of optimized virtual fields

It is possible to optimize the choice of virtual fields minimizing the error given in Eq. 12 in the same way as what was done for elasticity [12, 13]. These virtual fields are called "optimized virtual fields".

In Eq. 12, the error is made up of two terms, among which the first one is easily controllable by the choice of virtual fields. The noise effect is reduced when the virtual fields correspond to the minimum of the following functional:

$$\Psi_n = \sum_{j=1}^{n} g_j^2 = \sum_{j=1}^{n} \{U^*(t_n)\}^T [K(X_P, t_j)][K(X_P, t_j)]\{U^*(t_n)\} \tag{13}$$

However, the variance also involve the biases. Moreover, the bias of the cost function systematically affects the results and should be minimized by the choice of the virtual fields, simultaneously with Ψ_n.

As it was not possible to express a functional of the virtual fields for the bias, an empiric approach was adopted. It was noticed that the errors on $[K(X_P, t_j)]$ in elements with lower strains contributed more to the global bias of the cost function. The reason for this is that the larger the strains, the smaller their relative impact. Therefore, it would be beneficial to lower the contribution of these elements to the cost function defined in Eq. 13, particularly for low hardening materials.

For this purpose, it was thought to use an equation similar to Eq. 13 for defining the virtual fields, but with different weights attributed to the contribution of each finite element. Finite elements with small stress values should be penalized as they carry larger errors. Applying this weighting consists in changing the K matrix of Eq. 13 into $[K^\bullet]$ where the latter is defined as:

$$[K^\bullet(X_P, t_j)] = \sum_{i=1}^{I} \sigma_i^{eq}(t_j)[K_i^{el}(X_P, t_j)] \tag{14}$$

whereas the former was defined as:

$$[K(X_P, t_j)] = \sum_{i=1}^{I} [K_i^{el}(X_P, t_j)] \tag{15}$$

with $[K_i^{el}(X_P, t_j)]$ is the elementary stiffness matrix of element i and $\sigma_i^{eq}(t_j)$ the Von Mises equivalent stress at the centroid of element i.

Finally, the optimal virtual fields (OVF) at time t_n , denoted $\{U^*(t_n)\}$, that minimize the variance and the bias in the identification process, are defined as the minimum of the following functional:

$$\Psi_n^\bullet = \sum_{j=1}^{n} g_j^{\bullet 2} = \sum_{j=1}^{n} \{U^*(t_n)\}^T \underbrace{[K^\bullet(X_P, t_j)][K^\bullet(X_P, t_j)]}_{H_n} \{U^*(t_n)\} \tag{16}$$

The minimization of $\Psi_n^\bullet$ in Eq. 13 is carried out under the following constraints:

$$\begin{cases} U_x^* = 0; \quad U_y^* = 0 & \text{at the bottom} \\ U_x^* = 0; \quad U_y^* = L & \text{at the top} \end{cases} \tag{17}$$

where L is the distance from top to bottom of the region of interest.

The constraints in Eq. 17 are those used for a vertical tensile test. For other types of tests, these constraints may be changed. Indeed, the virtual fields must satisfy particular boundary conditions, such as to involve only the resultant load in the principle of virtual work since the distribution of tractions at the boundaries is unknown. Prescribing the constraint $U_y^* = L$ in Eq. 17 at the top boundary ensures that the trivial solution zero is avoided in minimizing Eq. 16.

Then, the optimal virtual fields will be obtained by minimizing $\Psi_n^\bullet$ in Eq. 16 under the constraints of Eq. 17. To solve this problem, the method of Lagrange multipliers is employed. It is a method that introduces a new unknown scalar variable, denoted λ (called the Lagrange multiplier) for each constraint, and defines a new cost function (called the Lagrangian) in terms of the original constraints and the Lagrange multipliers. The solution is obtained by inverting the system of equations written below:

$$\begin{bmatrix} [H_n] & [\Gamma]^T \\ [\Gamma] & [0] \end{bmatrix} \begin{Bmatrix} \{U^*(t_n)\} \\ \{\lambda\} \end{Bmatrix} = \begin{Bmatrix} \{0\} \\ 1 \end{Bmatrix} \tag{18}$$

where $[\Gamma]$ is a matrix which contains the constraints of Eq. 17.

The solution of Eq. 18 provides the virtual field that minimizes the influence of noise on the initial cost function defined in Eq. 7. For each stage t_n, Eq. 18 is updated and an optimal virtual field is deduced. Then, at each stage t_n, these optimal virtual fields are introduced in Eq. 7. Therefore, the influence of data noise onto the global $\Phi(X_P)$ cost function is minimized and the most robust identification is reached.

It must be remarked that solving Eq. 18 yields the optimized virtual fields necessary to deduce the constitutive parameters X_P. However, the problem is implicit because the unknown

constitutive parameters X_P are involved in the expression of $[H_n]$. This problem is solved by an iterative algorithm where the unknown parameters are replaced by their identified values. A first set of initial values is chosen. Tests have shown that this algorithm converges in about ten iterations whatever the choice of the initial values.

4. Validation on simulated data

4.1. Mechanical test

The objective now is to examine the efficiency of the above choice of virtual fields to minimize the effect of white noise on the identification. Firstly, simulated data are considered. The finite element package ANSYS was used to obtain these data. Assuming plane stress, the specimen which is investigated is a double-notched flat coupon and the loading is a uni-axial tensile-compression cycle (Fig. 1). The shape of the specimen is shown in Fig. 2. This geometry is similar to that already studied by Avril et al [11]. It leads to heterogeneous stress fields and is therefore an interesting test case for inverse approaches based on full-field measurements.

In the FE analysis, the boundary conditions were prescribed as follows: a total vertical displacement of 0.25 mm was prescribed at the top boundary using 50 sub-steps of 0.005 mm each for the first stage OA (tension), while the horizontal displacement was set to zero. The bottom boundary was clamped. During the second stage AB and the third stage BC, the boundary conditions were identical except that the vertical displacements of the top boundary were prescribed in the opposite direction with the same number of sub-steps (unloading and compression). During the last stage CD (unloading), again the same boundary conditions were used and a 0.035 mm total vertical displacement was prescribed on the top boundary, this time using 7 sub-steps of 0.005 mm. Therefore, 107 displacements maps have been eventually simulated just as if displacement fields were measured at 107 different times along the full test cycle in a real experiment. The advantage here is to estimate the effect of each load case (tension, unloading, compression, unloading) on the identification (the number 107 has been chosen to ensure displacement steps of ± 0.005 mm from one time step to another).

The material considered here is mild steel. Its properties are $X_1 = \nu = 0.3$, $X_2 = E = 210$ GPa for the elastic constants and $X_3 = \sigma_0 = 183.2$ MPa, $X_4 = H = 2460$ MPa, $X_5 = C = 1000$ MPa for respectively the yield stress, the isotropic hardening modulus and the

kinematic hardening parameter (Prager's linear kinematic hardening model was used here, see Appendix B).

In the FE analysis, 7200 elements were used in the area of interest of the specimen. The elements used are of type PLANE182, they are elements with four nodes having two degrees of freedom per node (translations) and use piecewise linear shape functions. They are used here in plane stress and incompressible plasticity. The nodal values of displacements in the area between the notches as well as the vertical load resultant were exported for each load step in an ASCII file for the identification procedure.

In order to simulate real experimental data, such as that provided by DIC [17, 18, 19, 20] or by the grid method [10, 11], displacement values at grid points were interpolated from the FE-simulated nodal displacement values. Interpolation was achieved using the function "griddata" in the Matlab software. The period of the grid over which data were interpolated is 0.1 mm, which is the same value as in [11] where real full-field data were measured with the grid method.

In order to improve the simulation realism, random Gaussian white noise has also been added to the displacement values interpolated at the grid points. Data will be processed without this additive noise for validating the identification approach and afterwards with the noise for quantifying the robustness of the identification approach. A random white noise was therefore added to each component of the displacement field, at each grid point where a datum is simulated. The distribution of this random white noise is Gaussian. Its expectation is zero and its standard deviation is denoted γ_u. In practice, γ_u is a scalar equal to the resolution of the measurement method.

To give a practical idea about γ_u, let us consider a test specimen with a rather common width of about 20 mm. Using CCD arrays of 1000 to 1200 pixels in the wider direction, a pixel size of 20 μm is generally required, leading to a sampling of 5 pixels per period of the 0.1 mm pitch grid, which is a typical value. With the grid method [10, 11], and a spatial resolution of 0.1 mm (equal to the grid pitch), it is typically possible to obtain γ_u=1/250 periods=0.4 μm. If digital image correlation is used, with subsets of 15 pixels (providing a spatial resolution of 0.3 mm), it is typically possible to obtain γ_u=0.02 pixels=0.4 μm [17, 18, 19, 20]. Therefore, γ_u=0.4 μm may be considered as a representative value for the noise standard deviation in the present situation. This requires however optimal settings in the optical set-up and camera. In

order to cover slightly larger errors in practice, a value of γ_u=0.5 μm was considered in this study. Noise with γ_u=1 μm will also be considered as a penalizing value to investigate the limits of the present approach.

4.2. Identification procedures

Identification routines were developed with the Matlab software in agreement with the equations shown in this paper. The principle described in Eq. 16 was implemented for finding the optimal virtual fields. The deduced $\Phi(X_P)$ cost function using these optimal virtual fields was minimized based on the Newton-Raphson procedure. In order to prove that the use of the optimized virtual fields (OVF) can increase the robustness of the identification process, four sets of manually defined virtual fields were also used to compute the cost function and minimize it. The functions used for defining these virtual fields are shown in Table 1, where L is the length of the area of interest and x and y are the horizontal and vertical coordinates.

4.3. Sensitivity analysis

The identification procedure was initially tested on the simulated data without noise. The VF2 virtual field (Table 1) was used for building up the cost function and solving the inverse problem. The idea was to investigate the effect of the loading path onto the identification results. Four loading paths were tested (see Fig. 1):

- only tension, denoted LP1 (number of sub-steps $n = 50$);
- tension-unloading, denoted LP2 (number of sub-steps $n = 57$);
- tension-unloading-compression, denoted LP3 (number of sub-steps $n = 100$);
- tension-unloading-compression-unloading, denoted LP4 (number of sub-steps $n = 107$).

For each load path, the objective is to retrieve the five unknown constitutive parameters defined previously. Results are reported in Table 2. It can be observed that for LP1, the plastic parameters are not all retrieved correctly. Only X_3 (yield stress) is identified accurately. The hardening parameters are erroneously identified because the development of plasticity in the case of monotonous tension does not allow to separate the contribution of isotropic and kinematic

hardening, which seems reasonable. The shape and the contour plots of the cost function for LP1 have been plotted in Fig. 3a, showing that the cost function exhibits a valley and thus has not a unique minimum.

The use of a tension-compression cycle (LP4) instead of monotonic tension (LP1) is the way of addressing this issue. The identified plastic parameters are in good agreement with their reference counterparts for both LP3 (n=100) and LP4 (n=107).

Indeed, on the one hand, the cumulated equivalent plastic strain continues to increase when switching from tension to compression. On the other hand, the directions of plastic flow are changed when switching from tension to compression. Consequently, one can distinguish the participation of each hardening parameter in the cost function. The sensitivity of the cost function to X_3 is higher than the sensitivity to X_4 and X_5: $\frac{\partial^2\Phi}{\partial X_3^2} = 80.96$, $\frac{\partial^2\Phi}{\partial X_4^2} = 0.0275$, $\frac{\partial^2\Phi}{\partial X_5^2} = 0.0107$. This is not surprising since the hardening modulus is much lower than the elastic modulus. The shape and the contour plots of the cost function have been plotted in Fig. 3b for LP4. It exhibits a unique minimum now. This shows that the use of a cyclic load is compulsory to identify constitutive parameters of a combined kinematic and isotropic hardening model.

4.4. Effect of data processing and field reconstruction

It has been shown that it is necessary to use load path LP4 to identify accurately all the parameters of the model from the data. Only this load path will be considered in the rest of the section.

4.4.1. Without noise (reconstruction accuracy)

Errors (in %) obtained in the identification of X_3, X_4 and X_5 from exact data have been plotted in Fig. 4. Different mesh sizes were used for defining the piecewise linear functions in the reconstruction process (data pre-processing). As exact data were used, only the effect of spatial resolution will be tested here. Indeed, the larger the mesh size, the smaller the number of piecewise linear functions in the basis of reconstruction functions. Consequently, the reconstruction will have a smoothing effect in the regions of high displacement gradients (or strain concentrations, at the notches in the present example). This smoothing effect will disturb the reconstructed fields and larger errors in the identified results are expected.

This effect is shown in Fig. 4. Errors for X_3, X_4 and X_5 have a tendency to increase with the mesh size, as expected.

The best result is obtained by using the smallest mesh size: 0.5 mm. Mesh sizes below 0.5 mm showed that it was not possible to improve the results. However, larger mesh sizes must be used in practice with noisy data for filtering purposes. This aspect is presented in the following section.

Deviations for X_5 are larger than for the other parameters. This may be induced by the particularly difficult case considered here where the kinematic hardening parameter is low, inducing a very low effect of kinematic hardening, hence a low sensitivity to this effect in the identification. Therefore, if the sensitivity is low, the identification procedure is less robust and deviates more when the data are disturbed, like here with the increasing mesh size. It was found that the identification of the kinematic parameter was better when this effect was more prominent but the computations for such cases are not presented here.

4.4.2. With noise (filtering effect on the reconstruction)

These results were obtained by running the identification process 30 times with different samples of noise. The 30 results of identification provide a distribution of identified parameters from which mean (or bias) and standard deviation can be computed. Fig. 5 shows the results for the γ_u=0.5 μm noise level, as a function of the mesh size. Fig. 6 reports the same information but for the γ_u=1 μm noise level

It can be noticed that the optimized virtual fields nearly systematically lead to the smallest bias (denoted deviation on the figures) and standard deviation. The effect is particularly spectacular for the large noise level. It can also be seen that the filtering effect is now competing with the reconstruction bias so that the errors are flatter with respect to mesh sizes. The larger the mesh size, the stronger the noise filtering (positive effect) but the worse the reconstruction error. A compromise has to be found. A mesh size of 1.3 mm will be used in the following.

4.5. Effect of the optimization of the virtual fields on the robustness

The final objective is to examine the influence of noise onto the identified parameters and to compare the results obtained by using the optimized virtual fields OVF1 with the results obtained by using the other virtual fields: VF2, VF3, VF4 and VF5.

The identified plastic parameters with each virtual field for load path LP4 are reported in Tables 3 and 4. They were identified using an iterative approach for minimizing the cost function in Eq. 7. A initial guess for the parameters is required for this procedure, here, the following were chosen: $X_3 = \sigma_0$=50 MPa, $X_4 = H$=4000 MPa, $X_5 = C$=3000 MPa. Different values were tried out, always leading to the same result. One can see that the results obtained using OVF1 are systematically more stable than the others. It is clear that the choice of virtual fields in Eq. 18 significantly improves the identification results. This is particularly spectacular for the X_5 parameter and the largest noise level. For lower noise levels, VF2 gives results that are very close to that obtained from OVF1, which proves here to be the best manually defined choice. It can be concluded that contrary to the case of linear elasticity, the optimization of the virtual fields is less critical to obtain good results, especially for good quality measurements.

5. Experimental procedure

5.1. Homogeneous tests

The material used in this study is an AISI 316L austenitic stainless steel. Its chemical composition in % of mass is: C: <0.027; Si: 0.61; Ni: 10-13; Cr: 16.5-18.5; Mo: 2.-2.5. The following components are also residually present: Ti, N, Cu.

The material is in the shape of 3 mm thick sheets. The specimens for the homogeneous and heterogeneous tests have been cut from the same plate. The dimensions of the specimen for the homogeneous tests are given by the NF A 03-151 standard and can be found in [10].

Six prismatic coupons were tested using the homogeneous test. The longitudinal specimen direction, *i.e.* the direction of loading, is denoted y and the perpendicular direction is denoted x. All the specimens were cut in the direction perpendicular to the sheet metal rolling direction, which means that the metal rolling direction is x. The longitudinal stress component σ_{yy} is the only component to be considered in the following and it is simply denoted σ. Strains ϵ_{xx} and ϵ_{yy} have been measured from bidirectional rosettes bonded back-to-back on the specimen to account for parasitic bending effects caused by grip misalignment. The stress σ is given by the ratio between the applied load and the cross sectional area of the specimen.

Each test consists in two stages of loading:

1. the first stage corresponds to increasing loads from zero to the maximum tensile load.
2. The second stage corresponds to decreasing loads just after the end of the first stage until the occurrence of buckling. Buckling is detected by comparing the difference of strains measured on the two faces of the specimen.

The stress-strain curves σ vs ϵ_{yy} are plotted in Fig. 7 and Fig. 8. In Fig. 7, only the first stage of loading is considered, whereas in Fig. 8 the response along the whole test has been plotted.

Young's modulus is deduced from the slope of the stress/strain curves in the linear part of the response. Poisson's ratio is deduced from the slope of the curves representing ϵ_{xx} vs ϵ_{yy}. The values are reported in Table 5. No difference has been noticed between the slopes of the strain/stress curves at the beginning of the test and at the beginning of the unloading just after the end of the first stage. This confirms that Young's modulus is not affected by the low strain values in the tests.

Regarding the plastic behaviour and hardening, two different analyzes were undertaken.

1. Considering tension only (monotonic loading), the behaviour can be modeled by Voce's model, which is suitable for modeling non linear hardening. The parameters of Voce's model that were deduced by curve fitting from the stress/strain curves are reported in Table 6.
2. Considering the whole test with tension and compression, Voce's model is not appropriate because the material exhibits a Bauschinger effect, with different elastic limits in tension and in compression after initial tensile loading in the plastic range. This type of behaviour can be modeled with the non-linear kinematic hardening (NLKH) model presented in Appendix B. A model with only three parameters proved to fit the experimental response with enough accuracy given the objectives of this study (validation of the identification approach). The parameters of the NLKH model that were deduced by curve fitting from the stress/strain curves are reported in Tab. 7.

The objective of this study is to prove that the material parameters that were identified using the stress/strain curves of the homogeneous tests (elastic parameters, Voce parameters, NLKH parameters) can also be deduced from the heterogeneous test using the VFM. The

consequences of this are essential: it means that elasto-plastic constitutive parameters, involving isotropic or kinematic hardening, can be identified without requiring standard shape specimens thanks to the present approach.

5.2. Heterogeneous tests

5.2.1. Mechanical arrangements

Six double-notched specimens were cut from the same plate as the one used for the previous tests. The dimensions of the double-notched specimens are shown in Fig. 9. As in the homogeneous tests, the longitudinal specimen direction, *i.e.* the direction of loading, is denoted y and the perpendicular direction is denoted x. As in the homogeneous tests, the metal rolling direction is x.

The objective of using a double-notched shape is to give rise to heterogeneous stress fields across the gauge area. This prevents the derivation of material parameters from a simple stress/strain curve analysis. Consequently, an inverse approach is mandatory for deriving the material parameters from such a configuration.

The double-notched specimens are loaded at a constant load rate of 2 kN per minute. It was checked that this load rate corresponded to very low strain rates in the specimen, below $10^{-4}\mathrm{s}^{-1}$. Therefore, all the visco-plastic effects were neglected in this study.

Six samples were tested using the heterogeneous test. Each test consists of two stages of loading.

1. The first stage corresponds to increasing loads from zero to the maximum tensile load which may vary from 19.5 to 23 kN in the six tests.
2. The second stage corresponds to decreasing loads just after the end of the first stage until the occurrence of buckling. The resulting maximum compression load may vary from 18 to 19.5 kN in absolute value in the six tests. A higher compression could not be reached because of buckling of the specimens. Buckling was detected by measuring the difference of strains between the two faces of the specimen (on one face, the strain is measured with the grid method, on the other, it is measured with a strain gauge).

5.2.2. Optical arrangements

A variety of full-field experimental techniques exist for measuring 2D displacement fields [21]. The grid method is the full-field measurement technique chosen here [22, 23]. It is a non-interferometric technique that uses a periodical encoding. The non-interferometric aspect of this technique is an asset for the simplicity of measurements. Compared to Digital Image Correlation techniques based on random patterns [18], the advantage of the grid method is that it provides a slightly better compromise between resolution and spatial resolution at the cost of bonding a grid onto the specimen. In this study, a grid period of pitch p=100μm was used, allowing a resolution of 0.35 μm and a spatial resolution of 0.18 mm. The high resolution (about p/300) here is obtained thanks to the good contrast of the black lines over the light shiny surface of the metal. Values of p/150 are typical for dark surfaces where the white glue provides the contrast.

The basic principle of the method is the following. A grid pattern is bonded onto the surface of the specimen following the procedure reported in [24]. It is considered as a spatial carrier having a phase value that varies spatially. The $u_x(x,y)$ and $u_y(x,y)$ displacement components relative to the unloaded configuration are calculated from the respective phase differences $\triangle\phi_x(x,y)$ (for vertical lines) and $\triangle\phi_y(x,y)$ (for horizontal lines) caused by the deformation (more details on these issues can be found in [22, 23]).

$$\begin{cases} u_x(x,y) = & -\dfrac{p}{2\pi}\triangle\phi_x(x,y) \\ u_y(x,y) = & -\dfrac{p}{2\pi}\triangle\phi_y(x,y) \end{cases} \tag{19}$$

where p is the period of the grid.

In this study, the field of view has a size of 24×20 mm^2. The images were taken using a Jai 8-bits camera with a CCD array of 1376×1024 pixels^2. Measurements were performed every second during the tests, which led to a number of measurements varying from 160 to 220 according to the test.

Displacement fields measured with the grid method during one of the six tests are displayed at different times in Fig. 11. They are symmetrical until the onset of buckling. The strain fields were derived from the displacement fields using a finite element reconstruction as explained in [25, 26] and in Appendix A. The strain fields deduced from the displacement fields

of Fig. 11 are reported in Fig. 12. The strain fields are heterogeneous, the plastic strains initially concentrating near the two circular notches and then spreading towards the centre of the specimen.

The influence of out of plane motions and residual bending were verified using a strain gauge on the other side of the specimen. The ϵ_{yy} curves measured by the gauge and on the opposite side by the grid method across the same strain gauge area are shown in Fig. 13 for one of the six tests. If out of plane effects were present, artifacts would be induced on the grid method [10] and the two curves would be different. Similarly, if bending occurs, the strain measured on both faces will be different and this will induce a difference between the two ϵ_{yy} curves.

The curves plotted in Fig. 13 show that there is a good agreement between ϵ_{yy} measured on both faces before the onset of buckling. This proves that the out of plane effects can be neglected in this test.

Finally, the ϵ_{yy} curves are also used for detecting the onset of buckling. Indeed, buckling results in bending strains, inducing large differences between ϵ_{yy} measured on both faces. Therefore, the ϵ_{yy} curves can also be used to determine the onset of buckling. The onset of buckling is the end of validity of the constant through-thickness stress assumption so the onset of buckling determined by the ϵ_{yy} curves is used to determine the last image with which the identification can still be achieved.

6. Experimental results

Once the displacement fields were obtained by the grid method, they were processed with the VFM as detailed in the first part of the paper. The optimal virtual fields as defined in Section 3 were used for the identification. The objective is to prove that the material parameters of the homogeneous tests are well retrieved even with the heterogeneous tests. The analysis is achieved at the two stages of the heterogeneous tests: first only for the monotonic loading stages, and then for the whole test.

6.1. Monotonic loading stage

6.1.1. Identification of the elastic parameters

The first step of the process is to identify the elastic parameters (Young's modulus and Poisson's ratio). The different strain fields measured before the onset of plasticity were determined and they were processed by the VFM to identify the elastic constants as described in [11]. The results are reported in Tab. 5. They are in agreement with the values obtained in the homogeneous tests. The values of the elastic parameters will now be used in the identification procedure for determining the plastic parameters.

6.1.2. Identification of the plastic parameters

The monotonic response of the material can be modeled with Voce's model. Therefore, the displacement fields measured in the first stage of the six heterogeneous tests have been processed through the VFM to identify the parameters of Voce's model. Results are reported in Table 6. They are in good agreement with their counterparts deduced from the homogeneous tests. The standard deviations are slightly larger in the heterogeneous tests.

Using the parameters identified in the heterogeneous tests, it is possible to model the tensile behaviour of the material and to compare the deduced stress/strain curves to the ones obtained in the homogeneous tests. The two types of curves are plotted in Fig. 7 for the first stage of loading (increasing loads). A good agreement is found between the two curves. The main discrepancies are located in the transition between linear elasticity and linear hardening.

6.2. Whole test analysis with the NLKH model

6.2.1. Identification of the elastic parameters

The identification of the elastic parameters was achieved again, this time using the displacement fields measured just after the end of the first stage of loading, while the load is decreasing and the material behaves elastically. Differences lower than 3% were reported between the elastic parameters identified in the unloading stage and the elastic parameters reported in Tab. 5. This confirms that no damage has occurred in the specimen during the tests. The elastic parameters that will be used further in the identification procedure for determining the plastic parameters are those reported in Tab. 5.

6.2.2. Identification of the plastic parameters for the NLKH model

The tension compression response of the material can be modeled with the NLKH model. Therefore, the displacement fields measured before the occurrence of buckling in the six heterogeneous tests have been processed through the VFM to identify the parameters of the NLKH model. The number of measurement times varies from 160 to 220 depending on the test. The end of the test, *i.e.* the occurrence of buckling, is detected when the ϵ_{yy} values measured on both sides of the specimen across the strain gauge area deviate by more than 10% (Fig. 13).

Results are reported in Table 7. They are in good agreement with their counterparts deduced from the homogeneous tests. The standard deviations are slightly larger in the heterogeneous tests.

Using the parameters identified in the heterogeneous tests, it is possible to model the tensile/compressive behaviour of the material and to compare the deduced stress/strain curves to the ones obtained in the homogeneous tests. The two types of curves are plotted in Fig. 8 for the whole tests considering increasing and decreasing loads. A good agreement is found between the two curves in the stage of decreasing loads. Discrepancies exist in the first stage of loading for increasing loads but they are attributed to the model itself which would have to be completed by other hardening terms in order to describe more faithfully the experimental tensile response of the material.

7. Discussion on experimental results

7.1. Monotonic loading stage

7.1.1. Sensitivity to the identified parameters

It was noted that the main discrepancies between the results of the homogeneous and heterogenous tests are located in the transition between linear elasticity and linear hardening. In Voce's model, the behaviour in the transition zone is driven by parameters R_0 and b. In order to check if the discrepancies can be accounted for by a low sensitivity of the response to R_0 and b in the heterogeneous tests, the sensitivity of the cost function used in the VFM to the material parameters was computed. For each parameter, the three others are fixed to their identified value, whereas the second order partial derivative of the cost function with regard

to the considered parameter is assessed. In order to provide dimensionless values, the partial derivatives are divided by the minimum values of the cost function. The results for one of the tests are the following:

$$\Phi'' = \begin{bmatrix} \frac{\partial^2\Phi}{\partial\sigma_0^2} = 0.0337 & \frac{\partial^2\Phi}{\partial\sigma_0\partial R_0} = 0.00014 & \frac{\partial^2\Phi}{\partial\sigma_0\partial R_{inf}} = 0.029 & \frac{\partial^2\Phi}{\partial\sigma_0\partial b} = 0.00014 \\ \frac{\partial^2\Phi}{\partial R_0\partial\sigma_0} = 0.00014 & \frac{\partial^2\Phi}{\partial R_0^2} = 0.000001 & \frac{\partial^2\Phi}{\partial R_0\partial R_{inf}} = 0.00014 & \frac{\partial^2\Phi}{\partial R_0\partial b} = 0.0000009 \\ \frac{\partial^2\Phi}{\partial R_{inf}\partial\sigma_0} = 0.029 & \frac{\partial^2\Phi}{\partial R_{inf}\partial R_0} = 0.00014 & \frac{\partial^2\Phi}{\partial R_{inf}^2} = 0.0263 & \frac{\partial^2\Phi}{\partial R_{inf}\partial b} = 0.0001 \\ \frac{\partial^2\Phi}{\partial b\partial\sigma_0} = 0.00014 & \frac{\partial^2\Phi}{\partial b\partial R_0} = 0.0000009 & \frac{\partial^2\Phi}{\partial b\partial R_{inf}} = 0.0001 & \frac{\partial^2\Phi}{\partial b^2} = 0.0000009 \end{bmatrix}$$

The results show that the most sensitive parameter (which must be the best identified) is the initial elastic limit σ_0. Then comes R_{inf} which coupled to σ_0 corresponds to the intersection of the horizontal asymptote with the ordinate axis. Then comes the slope of the horizontal asymptote R_0 and finally parameter b which exhibits the smallest sensitivity.

Parameter b describes only the curvature of the small transition zone after the onset of plasticity and as the slope of the horizontal asymptote is smaller than that of the linear part (low hardening), the influence of b and R_0 is smaller on the function cost.

However, the sensitivity table shows that the response is still sensitive to parameter b. Consequently, there is no real sensitivity issue in the identification problem solved here. This conclusion is also in agreement with the fairly good repeatability between the different stress/strain curves plotted with the identified parameters.

This means that the differences between the homogeneous and the heterogeneous stress/strain curves plotted in Fig. 7 cannot be attributed to an absence of sensitivity to the behaviour in the transition zone. Therefore, it may be concluded that the behaviour in the transition zone is different between the homogeneous and heterogeneous tests. This may be true because in the homogeneous test, the stress/strain curve represents the global response whereas in the heterogeneous test, the stress/strain curve represents the local material behaviour. The trends show a shorter transition zone in the local behaviour. This was also experienced in [10] where b was somewhat smaller when it was identified with the VFM compared to homogeneous tests. This may show one of the limitations of standard procedures that tend to smooth out the material's response.

7.1.2. Influence of the initial parameters

The VFM is based on the minimization of a cost function. For a non-convex cost function there is no certainty to reach the global minimum. The solution may therefore be sensitive to the initial values selected to initiate the minimization procedure. This may explain the larger standard deviations of the parameters identified from the heterogeneous tests. In order to check the importance of this issue, different starting values of the parameters were selected in the range of physical meaning. Such sets of values were tested to initialize the identification procedure. All led to the same results (with less than 0.05% difference). This confirms the uniqueness of the solution and the independence of the solution to the initial values.

7.1.3. Influence of the choice of the virtual fields

An important aspect emphasized in the first part of this paper is the choice of the virtual fields in the identification procedure. In order to prove the superiority of the optimal virtual fields presented here, the virtual fields reported in Tab. 1 were used to process the data from the heterogeneous tests. Results are reported in Tab. 8. They prove that the best agreement with the material parameters of the homogeneous tests is obtained with the optimal virtual fields. This confirms the very positive filtering effect of the optimal virtual fields that was noticed with simulated data .

7.2. Whole test analysis with the NLKH model

7.2.1. Sensitivity of the identified parameters

It was noted that significant discrepancies existed between the stress/strain curves deduced from the homogeneous and heterogenous tests at the onset of plasticity in the first stage (increasing tensile load). The onset of plasticity is driven in the NLKH model by parameter σ_0. In order to check if the discrepancies may be explained by a lack of sensitivity to parameter σ_0, a sensitivity study was achieved. The sensitivities of the VFM cost function to the parameters of the NLKH model are reported in the following table:

$$\Phi'' = \begin{bmatrix} \frac{\partial^2\Phi}{\partial\sigma_0^2} = 0.295 & \frac{\partial^2\Phi}{\partial\sigma_0\partial C} = 0.0007 & \frac{\partial^2\Phi}{\partial\sigma_0\partial\gamma} = 0.027 \\ \frac{\partial^2\Phi}{\partial C\partial\sigma_0} = 0.0007 & \frac{\partial^2\Phi}{\partial C^2} = 0.000004 & \frac{\partial^2\Phi}{\partial C\partial\gamma} = 0.0003 \\ \frac{\partial^2\Phi}{\partial\gamma\partial\sigma_0} = 0.027 & \frac{\partial^2\Phi}{\partial\gamma\partial C} = 0.0003 & \frac{\partial^2\Phi}{\partial\gamma^2} = 0.029 \end{bmatrix}$$

The results show that parameter σ_0 exhibits the largest sensitivity. The sensitivity to γ and C is significant. Consequently, there is no sensitivity issue in the identification problem solved here. This conclusion is also in agreement with the fairly good repeatability between the different stress/strain curves plotted with the identified parameters.

This means that the differences between the homogeneous and the heterogeneous stress/strain curves plotted in Fig. 7 cannot be attributed to an absence of sensitivity to the behaviour at the beginning of the plastic flow. A possible explanation of the difference between the homogeneous and the heterogeneous stress/strain curves may be attributed to the model itself. Indeed, the NLKH model used here has only three parameters and it is dedicated to reproducing the plastic behaviour in compression after one cycle of loading and unloading.

7.2.2. Influence of the initial parameters

Several sets of initial parameters drawn within a large range of physically plausible values have been tested to check the influence of initialization on the minimization of the cost function. The same results were systematically obtained with a difference of less than 0.05%. This confirms that there were no uniqueness issues in the identification problem.

7.2.3. Influence of the choice of the virtual fields

An important aspect is the choice of the virtual fields in the identification procedure. In order to prove the superiority of the optimal virtual fields presented here, the virtual fields reported in Tab. 1 were used to process the data from the heterogeneous tests. Results are shown in Tab. 9. They prove that the best agreement with the material parameters of the homogeneous tests is obtained with the optimal virtual fields. This is also confirmed by comparing the different responses modeled with the identified parameters (Fig. 14). The stress/strain curve modeled with the parameters that were identified with the optimal virtual fields is the response that has the best agreement with the stress/strain curve of the homogeneous test. This confirms the beneficial filtering effect of the optimal virtual fields that was noticed with the simulated data. It should be noted however that the benefit of the optimized virtual fields is less spectacular than for Voce's model. This is probably caused by the lower number of parameters to identify in the NLKH model. Future work will include the use of more complex isotropic and/or hardening

laws to check the stability of the procedure and try to improve the description of the onset of plasticity in the cyclic tests.

8. Conclusion

In this paper, the extension of the virtual fields method to combined isotropic and kinematic hardening has been addressed. It is clear that the use of the cyclic load is indispensable to identify constitutive parameters in this case. The choice of optimal virtual fields has been investigated. It is based on the effect of noisy data to the cost function. The optimized virtual fields significantly improve the identification results which opens the way to the identification of more sophisticated elasto-plastic constitutive models: anisotropy, larger strains, material heterogeneities. The Newton-Raphson method was also introduced for the minimization of the cost function, thus reducing computation time.

The experimental validation was performed on an AISI 316L stainless steel material. Standard homogeneous tests were performed on specimens equipped with strain gauges to derive the reference uniaxial stress-strain curve. Then heterogeneous tests on double-notched coupons were performed. Full-field measurements were obtained through the grid method all along the specimen loading which consisted in a first tensile stage followed by unloading and compression until buckling occurred. These displacements maps were then processed by the Virtual Fields Method to identify a Voce's model for the loading part and a non linear kinematic hardening model combined with linear isotropic hardening for the complete loading cycle. Results were very satisfactory and the improvement brought by the optimized virtual fields clearly demonstrated.

Future work will include the adaptation of the procedure to large deformations, following initial validation of the VFM in hyperelasticity [15, 16], to heterogeneous materials such as welds (feasibility study in [27]) and to more complex constitutive laws, including visco-plasticity in the same spirit as a first recent study [28]. The final objective is to implement these routines into a GUI-based software to provide to the mechanics of materials community.

Acknowledgments

The authors are grateful to the Champagne Ardenne Regional Council for funding the PhD grant of Vinh The TRAN. This work is also part of the Photofit project (Grant ANR-05-

BLAN- 0327-01) funded by the ANR (French National Research Agency).

Appendix A

Reconstruction principle of the displacement fields from data provided at grid points

In order to expand the virtual fields as piecewise bilinear functions, the region of interest is meshed with quadrangular or triangular elements. Triangles are used here because they are simple and they can easily fit any shape. One writes the displacement fields starting from displacements at the nodes of the grid by using the following basis of piecewise linear shape functions:

$$\begin{cases} u_x(x,y) = & N_1(x,y)u_x(A_1) + N_2(x,y)u_x(A_2) + N_3(x,y)u_x(A_3) = \langle N(x,y)\rangle\{U_x^e\} \\ u_y(x,y) = & N_1(x,y)u_y(A_1) + N_2(x,y)u_y(A_2) + N_3(x,y)u_y(A_3) = \langle N(x,y)\rangle\{U_y^e\} \end{cases} \tag{20}$$

where $u_x(x,y)$, $u_y(x,y)$ are the displacements measured at the nodes, $N_n(x,y)$ are the classical bilinear shape functions of triangular finite elements. $\{U_x^e\}$ and $\{U_y^e\}$ are the column vectors composed of the three nodal displacements $u_x(A_n)$ and $u_y(A_n)$, $\langle N(x,y)\rangle$ is a row vector composed of the three shape functions.

From Eq. 20 one can evaluate the nodal displacements starting from the experimental values $u_x(x,y)$, $u_y(x,y)$ by regression in the least square sense. Once nodal displacements are obtained, one can rebuild the field of approximate displacements by using the shape functions (Eq. 20). Differentiating the $\langle N_n(x,y)\rangle$ basis functions provides strain fields which are constant in each triangle.

$$\boldsymbol{\epsilon}_{el} = [B_1\ B_2\ B_3]\{U_{el}\} \tag{21}$$

$$= [B_{el}]\{U_{el}\} \tag{22}$$

with: $\{U_{el}\} = \begin{Bmatrix} u_x(A_1) \\ u_y(A_1) \\ u_x(A_2) \\ u_y(A_2) \\ u_x(A_3) \\ u_y(A_3) \end{Bmatrix}$; $\boldsymbol{\epsilon}_{el} = \begin{Bmatrix} \boldsymbol{\varepsilon}_{xx} \\ \varepsilon_{yy} \\ 2\varepsilon_{xy} \end{Bmatrix}$ is the vector of the strains in each element;

each matrix $[B_i](i = 1, 2, 3)$ containing the gradients of the shape functions N_i on each element is given by:

$$[B_i] = \begin{bmatrix} \frac{\partial N_i}{\partial x} & 0 \\ 0 & \frac{\partial N_i}{\partial y} \\ \frac{\partial N_i}{\partial y} & \frac{\partial N_i}{\partial x} \end{bmatrix} \tag{23}$$

The constant values above are then averaged at each node so as to provide nodal values of the strain components. Eventually, the whole strain fields are reconstructed with the piecewise linear basis functions. However, only the nodal displacements $\{U_x^e\}$ and $\{U_y^e\}$ are used further for the identification. They are collected as vectors denoted $\{\dot{U}(t)\}$, that are the displacement increment fields measured at each measurement times t during a test. The same basis of piecewise bilinear functions are used for the virtual fields. One obtains:

$$\begin{aligned} \boldsymbol{\epsilon}_{el}^* &= [B_1\ B_2\ B_3]\ \{U_{el}^*\} \\ &= [B_{el}]\ \{U_{el}^*\} \end{aligned} \tag{24}$$

where $[B_{el}]$ is a matrix containing the gradients of the shape functions of the triangular linear element and $\{\boldsymbol{\epsilon}_{el}^*\}$ is the virtual strain field.

Appendix B

Constitutive equations considered in this study

Several assumptions have been made in this study:

- small perturbations,
- plane stress,
- isotropy in elasticity and plasticity,
- volume conservation in plasticity,
- time independent plasticity.

Plasticity is characterized by the irreversible strain that occurs in a material once a certain level of stress is reached. The theory of this constitutive law provides a mathematical relationship that characterizes the elasto-plastic response of the materials. There are three ingredients in the rate-independent plasticity theory [29]: the yield criterion, the flow rule and the hardening rule as:

1. Yield criterion

The yield criterion f defines the limits of the linear elastic domain. Different yield criteria exist in isotropic plasticity. The Von-Mises criterion is used here, which is based on the equivalent stress, denoted σ_{eq}, R the isotropic hardening variable and σ_0 the initial yield stress:

$$f = \sigma_{eq} - R - \sigma_0 \leq 0 \tag{25}$$

$$\sigma_{eq} = \left[\frac{3}{2}(\underline{\underline{\sigma}}' - \underline{\underline{X}}) : (\underline{\underline{\sigma}}' - \underline{\underline{X}})\right]^{\frac{1}{2}} \tag{26}$$

where $\underline{\underline{\sigma}}'$ is the deviatoric stress tensor and $\underline{\underline{X}}$ is the yield surface translation tensor (location of the centre of the yield surface describing kinematic hardening). They are defined as follows in plane stress conditions:

$$\underline{\underline{\sigma}}' = \begin{bmatrix} s_{xx} & s_{xy} & 0 \\ s_{xy} & s_{yy} & 0 \\ 0 & 0 & s_{zz} \end{bmatrix} \quad \text{with} \quad s_{zz} = -(s_{xx} + s_{yy})$$

$$\begin{Bmatrix} s_{xx} \\ s_{yy} \\ s_{xy} \end{Bmatrix} = \begin{Bmatrix} 2\sigma_{xx}/3 - \sigma_{yy}/3 \\ 2\sigma_{yy}/3 - \sigma_{xx}/3 \\ 2\sigma_{xy} \end{Bmatrix} \tag{27}$$

$$\underline{\underline{X}} = \begin{bmatrix} X_{xx} & X_{xy} & 0 \\ X_{xy} & X_{yy} & 0 \\ 0 & 0 & X_{zz} \end{bmatrix}; \quad X_{zz} = -(X_{xx} + X_{yy}) \tag{28}$$

When σ_{eq} is equal to the current yield stress of the material, $R+\sigma_0$, the material develops plastic strains. If σ_{eq} is less than $R+\sigma_0$, the material is elastic and the stresses develop according to the elastic stress-strain relations.

2. Flow rule

The flow rule determines the direction of plastic straining and is given as:

$$\underline{\underline{\dot{\varepsilon}}}^p = \dot{\lambda} \frac{\partial f}{\partial \underline{\underline{\sigma}}} \tag{29}$$

where $\dot{\lambda}$ is the plastic multiplier (which determines the amount of plastic straining). The flow rule here is termed associative and the plastic strains occur in a direction normal to the yield surface (classical assumption).

3. Hardening rule

The hardening rule describes the changing of the yield surface with progressive yielding, so that the conditions for subsequent yielding can be established.

In isotropic hardening, the yield surface remains centred on its initial centerline and expands in size as the plastic strains develop. This can be written as (for a linear isotropic hardening law):

$$R(p) = Hp \tag{30}$$

where H is the hardening modulus and p the cumulated equivalent plastic strain:

$$p = \int_0^t \sqrt{\frac{2}{3}\dot{\underline{\underline{\varepsilon}}}^p(\tau) : \dot{\underline{\underline{\varepsilon}}}^p(\tau)}d\tau \tag{31}$$

If Voce's non linear hardening model is considered:

$$R(p) = R_0 p + R_{inf}[1 - exp(-bp)] \tag{32}$$

where R_0 is the asymptotic hardening modulus and R_{inf} and b are the parameters describing the non linear part in the initial yield zone.

In kinematic hardening, it is assumed that the yield surface remains constant in size and the surface translates in the stress space with progressive yielding. If Prager's linear hardening model is considered:

$$\dot{\underline{\underline{X}}}(\underline{\underline{\varepsilon}}^p) = C\dot{\underline{\underline{\varepsilon}}}^p \tag{33}$$

where C is a material parameter.

If the non linear kinematic hardening model is considered (NLKH):

$$\dot{\underline{\underline{X}}}(\underline{\underline{\varepsilon}}^p) = C\dot{\underline{\underline{\varepsilon}}}^p - \gamma\underline{\underline{X}}\dot{p} \tag{34}$$

where C and γ are material parameters.

4. Expression of the measured total strain rate $\dot{\boldsymbol{\epsilon}}$ as a function of the stress rate $\dot{\boldsymbol{\sigma}}$

A plastic flow occurs when two conditions are satisfied simultaneously:

1. the stresses are already on the yield surface, meaning that the yield function is null (Eq. 25);

2. the stresses remain on the yield surface, meaning that the yield function remains null:

$$df = \frac{\partial f}{\partial \underline{\underline{\sigma}}} : \underline{\underline{\dot{\sigma}}} + \frac{\partial f}{\partial \underline{\underline{X}}} : \underline{\underline{\dot{X}}} + \frac{\partial f}{\partial p}\dot{p} = 0 \tag{35}$$

In plane stress, Eq. 35 (also called the consistency condition) becomes:

$$df = \boldsymbol{S} \cdot \dot{\boldsymbol{\sigma}} - \boldsymbol{S1} \cdot \dot{\boldsymbol{X}} - \frac{\partial R}{\partial p}\dot{p} = 0 \tag{36}$$

where

$$\dot{\boldsymbol{X}} = \left\{ \begin{array}{l} \dot{X}_{xx} \\ \dot{X}_{yy} \\ \dot{X}_{xy} \\ \dot{X}_{zz} = -(\dot{X}_{xx} + \dot{X}_{yy}) \end{array} \right\}; \quad \dot{p} = \left[\frac{2}{3} \{ (\dot{\varepsilon}^p_{xx})^2 + (\dot{\varepsilon}^p_{yy})^2 + (\dot{\varepsilon}^p_{xx} + \dot{\varepsilon}^p_{yy})^2 + 2(\dot{\varepsilon}_{xy} p)^2 \} \right]^{\frac{1}{2}} \tag{37}$$

and

$$\boldsymbol{S} = \left\{ \begin{array}{l} \frac{\partial f}{\partial \sigma_{xx}} \\ \frac{\partial f}{\partial \sigma_{yy}} \\ 2\frac{\partial f}{\partial \sigma_{xy}} \end{array} \right\} = \frac{3}{2\sigma_{eq}} \left\{ \begin{array}{l} s_{xx} - X_{xx} \\ s_{yy} - X_{yy} \\ 2(s_{xy} - X_{xy}) \end{array} \right\}; \boldsymbol{S1} = \left\{ \begin{array}{l} \frac{\partial f}{\partial X_{xx}} \\ \frac{\partial f}{\partial X_{yy}} \\ 2\frac{\partial f}{\partial X_{xy}} \\ \frac{\partial f}{\partial X_{zz}} \end{array} \right\} = \frac{3}{2\sigma_{eq}} \left\{ \begin{array}{l} s_{xx} - X_{xx} \\ s_{yy} - X_{yy} \\ 2(s_{xy} - X_{xy}) \\ s_{zz} - X_{zz} \end{array} \right\} \tag{38}$$

where the "2" is the coefficient coming from the transformation of the contracted product of tensors into the scalar product of vectors.

According to the flow rule Eq. 29 with $\dot{p} = \dot{\lambda}$ and to the non linear kinematic hardening laws, one gets:

$$\begin{aligned} \dot{\boldsymbol{X}} &= C \frac{3\dot{\lambda}}{2\sigma_{eq}} \underbrace{\left\{ \begin{array}{l} s_{xx} - X_{xx} \\ s_{yy} - X_{yy} \\ s_{xy} - X_{xy} \\ s_{zz} - X_{zz} \end{array} \right\}}_{\boldsymbol{s2}} - \dot{\lambda}\gamma \underbrace{\left\{ \begin{array}{l} X_{xx} \\ X_{yy} \\ X_{xy} \\ X_{zz} \end{array} \right\}}_{\boldsymbol{X}} \\ &= C\dot{\lambda}\boldsymbol{S2} - \dot{\lambda}\gamma\boldsymbol{X}; \quad \text{with} \quad \boldsymbol{S2} = \frac{3}{2\sigma_{eq}}\{\boldsymbol{s2}\} \end{aligned} \tag{39}$$

Therefore, by using Eq. 39 and introducing the linear isotropic hardening law, Eq. 36 becomes:

$$df = \boldsymbol{S} \cdot \dot{\boldsymbol{\sigma}} - \dot{\lambda} \left(C \underbrace{\boldsymbol{S1} \cdot \boldsymbol{S2}}_{=\frac{3}{2}} - \gamma \boldsymbol{S1} \cdot \boldsymbol{X} \right) - H\, \dot{\lambda} = 0 \tag{40}$$

So:

$$\dot{\lambda} = \frac{\boldsymbol{S} \cdot \dot{\boldsymbol{\sigma}}}{[\frac{3}{2}C - \gamma \boldsymbol{S1} \cdot \boldsymbol{X}] + H} \tag{41}$$

Decomposing the total strain in its elastic and plastic parts and introducing Hooke's law in plane stress, one gets:

$$\dot{\boldsymbol{\sigma}} = [Q](\dot{\boldsymbol{\epsilon}} - \dot{\boldsymbol{\epsilon}}^p) = [Q](\dot{\boldsymbol{\epsilon}} - \dot{\lambda}\boldsymbol{S}) \tag{42}$$

According to Eq. 41, Eq. 42 can finally be defined:

$$\begin{Bmatrix} \dot{\sigma}_{xx} \\ \dot{\sigma}_{yy} \\ \dot{\sigma}_{xy} \end{Bmatrix} = \underbrace{\left[[Q]^{-1} + \frac{\boldsymbol{S} \bigotimes \boldsymbol{S}}{\left(\frac{3}{2}C - \gamma \boldsymbol{S1} \cdot \boldsymbol{X}\right) + H} \right]^{-1}}_{\text{tangent stiffness matrix } [M]} \begin{Bmatrix} \dot{\varepsilon}_{xx} \\ \dot{\varepsilon}_{yy} \\ 2\dot{\varepsilon}_{xy} \end{Bmatrix} \tag{43}$$

References

[1] S. Avril, M Bonnet, A.-S. Bretelle, M. Grédiac, F. Hild F., P. Ienny P, F. Latourte, D. Lemosse, S. Pagano, E. Pagnacco, and F. Pierron. Overview of identification methods of mechanical parameters based on full-field measurements. *Experimental Mechanics*, 48(4):381–402, 2008.

[2] M.H.H. Meuwissen, C.W.J. Oomens, F.P.T. Baaijens, R. Petterson, and J.D. Janssen. Determination of the elasto-plastic properties of aluminium using a mixed numerical-experimental method. *Journal of Materials Processing Technology*, 75:204–211, 1998.

[3] J. Kajberg and G. Lindkvist. Characterization of materials subjected to large strains by inverse modelling based on in-plane displacement fields. *International Journal of Solids and Structures*, 41:3439–3459, 2004.

[4] J. Kajberg, K.G. Sundin, L.G. Melin, and P. Ståhle. High strain rate tensile and viscoplastic parameter identification using micoscopic high-speed photography. *International Journal of Plasticity*, 20:561–575, 2004.

[5] J. Kajberg and B. Wikman. Viscoplastic parameter estimation by high strain-rate experiments and inverse modelling - speckle measurements and high-speed photography. *International Journal of Solids and Structures*, 44:145–164, 2007.

[6] F. Latourte, A. Chrysochoos, S. Pagano, and B. Wattrisse. Elastoplastic behavior identification for heterogeneous loadings and materials. *Experimental Mechanics*, 48(4):435–449, 2008.

[7] S. Cooreman, D. Lecompte, H. Sol, J. Vantomme, and D. Debruyne. Identification of mechanical material behaviour through inverse modeling and DIC. *Experimental Mechanics*, 48(4):421–433, 2008.

[8] L. Geng, Y. Shen, and R.H. Wagoner. Anisotropic hardening equations derived from reverse-bend testing. *International Journal of Plasticity*, 18(5-6):743–767, 2002.

[9] M. Grédiac and F. Pierron. Applying the virtual fields method to the identification of elasto-plastic constitutive parameters. *International Journal of Plasticity*, 22:602–627, 2006.

[10] Y. Pannier, S. Avril, R. Rotinat, and F. Pierron. Identification of elasto-plastic constitutive parameters from statically undetermined tests using the virtual fields method. *Experimental Mechanics*, 46(6):735–755, 2006.

[11] S. Avril, F. Pierron, Y. Pannier, and R. Rotinat. Stress reconstruction and constitutive parameter identification in elastoplasticity using measurements of deformation fields. *Experimental Mechanics*, 48(4):403–419, 2008.

[12] S. Avril and F. Pierron. General framework for the identification of elastic constitutive parameters from full-field measurements. *International Journal of Plasticity*, 44:4978–5002, 2007.

[13] S. Avril, M. Grédiac, and F. Pierron. Sensitivity of the virtual fields method to noisy data. *Computational Mechanics*, 34:439–452, 2004.

[14] D. Chapelle and M. Darrieulat. The occurence of shear banding in a millimeter scale (123)[634] grain of an Al-4.5% Mg alloy during plane strain compression. *Materials Science and Engineering A*, 347(1-2):32–41, 2003.

[15] N. Promma, B. Raka, M. Grédiac, E. Toussaint, J.-B. Le Cam, X. Balandraud, and F. Hild. Application of the virtual fields method to mechanical characterization of elastomeric materials. *International Journal of Solids and Structures*, 46(3-4):698–715, 2009.

[16] T. Guélon, E. Toussaint, J.-B. Le Cam, N. Promma, and M. Grédiac. A new characterisation method for rubber. *Polymer Testing*, 2009. In press.

[17] G. Besnard, F. Hild, and S. Roux. "Finite element" displacement fields analysis from digital images: application to Portevin-Le Châtelier bands. *Experimental Mechanics*, 46:789–803, 2006.

[18] H. Schreier and M.A. Sutton. Systematic errors in digital image correlation due to undermatched subset shape functions. *International Journal of Plasticity*, 42:303–310, 2002.

[19] S. Belhabib, H. Haddadi, M. Gasperini, and P. Vacher. Heterogeneous tensile test on elastoplastic metallic sheets: Comparison between fem simulations and full-field strain measurements. *International Journal of Mechanical Sciences*, 50(1):14–21, 2008.

[20] E. Toussaint, M. Grédiac, and F. Pierron. The virtual fields method with piecewise virtual fields. *International Journal of Mechanical Sciences*, 48(3):256–264, 2006.

[21] Rastogi P. *Photomechanics*. Springer Verlag, 1999.

[22] Y. Surrel. Moiré and grid methods: a signal processing approach. In Ryszard J. Pryputniewicz and Jacek Stupnicki, editors, *Interferometry '94: Photomechanics*, volume 2342, pages 213–220. The International Society for Optical Engineering, SPIE, Nov 1994.

[23] S. Avril, E. Ferrier E, P. Hamelin, Y. Surrel, and A. Vautrin. A full-field optical method for the experimental analysis of reinforced concrete beams repaired with composites. *Composites Part A*, 35(7-8):873–884, 2004.

[24] J.-L. Piro and M. Grédiac. Producing and transferring low-spatial-frequency grids for measuring displacement fields with moiré and grid methods. *Experimental Techniques*, 28(4):23–26, 2004.

[25] Z. Feng and R.E. Rowlands. Smoothing finite-element and experimental hybrid technique for stress analyzing composites. *Computers and Structures*, 6:631–639, 1991.

[26] S. Avril, P. Feissel, F. Pierron, and P. Villon. Estimation of strain field from full-field displacement noisy data. *European Journal of Computational Mechanics*, 17(5-7):857–868, 2008.

[27] M.A. Sutton, J. Yan, S. Avril, F. Pierron, and S. Adeeb. Identification of heterogeneous constitutive parameters in a welded specimen: Uniform stress and virtual fields methods for material property estimation. *Experimental Mechanics*, 48(4):451–464, 2008.

[28] S. Avril, F. Pierron, J. Yan, and M.A. Sutton. Identification of viscoplastic parameters and characterization of lders behavior using digital image correlation and the virtual fields method. *Mechanics of Materials*, 40(9):729–742, 2008.

[29] Lemaître J. and Chaboche J.-L. *Mechanics of solid materials*. Cambridge University Press, Cambridge, UK, 1990.

	OVF1	VF2	VF3	VF4	VF5
U_x	Eq 16	0	0	$x^{1/27} \mid sin(y(y-L)) \mid$	$x^{1/27}y^{1/27} \mid sin(y(y-L)) \mid$
U_y	Eq 16	y	$1-e^{y/L}$	$sin\left(\frac{y\pi}{2L}\right)$	$y^{1/2}$

Table 1: Different sets of virtual fields for comparison purposes.

	Ref	LP 1	LP 2	LP 3	LP 4
$X_1 = \nu$	0.3	0.3	0.3	0.3	0.3
$X_2 = E$ (GPa)	210	209.8	209.8	209.8	209.8
$X_3 = \sigma_0$ (MPa)	183.2	183.6	183.6	183.5	183.4
$X_4 = H$ (GPa)	2.46	3.02	2.07	2.47	2.47
$X_5 = C$ (GPa)	1	0.61	4.24	0.99	0.993

Table 2: Identified parameters for different load paths.

	Coefficient of variation (%)					Deviation (%)				
	OVF1	VF2	VF3	VF4	VF5	OVF1	VF2	VF3	VF4	VF5
$X_3 = \sigma_0$ (MPa)	0.36	0.23	0.25	0.56	1.03	0.88	1.61	1.64	0.99	0.45
$X_4 = H$ (GPa)	1.93	1.76	2	3.63	7.46	3.6	7.32	6.97	5.67	4.6
$X_5 = C$ (GPa)	6.53	10.05	10.43	10.2	14.3	2.83	2.72	2.43	9.64	12.7

Table 3: Comparison of errors with different virtual fields from noisy data with the 0.5 μm noise level (mesh size 1.3 mm, pitch of the grid 100 μm).

	Coefficient of variation (%)					Deviation (%)				
	OVF1	VF2	VF3	VF4	VF5	OVF1	VF2	VF3	VF4	VF5
$X_3 = \sigma_0$ (MPa)	0.55	0.47	0.55	1.02	1.94	0.09	3.95	4.1	3.2	3.2
$X_4 = H$(GPa)	4	6.87	7.76	11.2	23.8	1.56	19.3	19.2	18.4	19.7
$X_5 = C$(GPa)	14.4	17.3	18.3	18.7	29.5	38.3	63.4	64.1	79.6	88.5

Table 4: Comparison of errors with different virtual fields from noisy data with the 1 μm noise level (mesh size 1.3 mm, pitch of the grid 100 μm).

	Homogeneous tests	Heterogeneous tests
	Average $\pm 2\times$ Standard Deviation	Average $\pm 2\times$ Standard Deviation
E(GPa)	199 ± 7	197.6 ± 7
ν	0.299 ± 0.012	0.307 ± 0.018

Table 5: Identified elastic parameters.

	Homogeneous tests	Heterogeneous tests
	Average $\pm 2\times$ Standard Deviation	Average $\pm 2\times$ Standard Deviation
σ_0(MPa)	179.8 ± 28	183.2 ± 55
R_0(GPa)	3.17 ± 0.8	3.29 ± 1.5
R_{inf}(MPa)	120.4 ± 29	120.8 ± 49
$b(\times 10^3)$	2.44 ± 0.83	2.23 ± 1

Table 6: Identified plastic parameters for Voce's model.

	Homogeneous tests	Heterogeneous tests
	Average $\pm 2\times$ Standard deviation	Average $\pm 2\times$ Standard deviation
σ_0(MPa)	198.1 ± 7	203.6 ± 13
C(GPa)	30.7 ± 6	29.6 ± 3
γ	292 ± 52	262.4 ± 53

Table 7: Identified plastic parameters for the NLKH model.

	Homogeneous test	Heterogeneous test			
		OVF1	VF2	VF3	VF4
	Av. $\pm$ 2 std.	Av. $\pm$ 2 std.	Av. $\pm$ 2 std.	Av. $\pm$ 2 std.	Av. $\pm$ 2 std.
σ_0(MPa)	179.8 ± 28	183.2 ± 55	171.1 ± 74	186.7 ± 48	78 ± 135
R_0(GPa)	3.17 ± 0.8	3.29 ± 1.5	4.3 ± 2	4.1 ± 2.1	3.2 ± 1.8
R_{inf}(MPa)	120.4 ± 29	120.8 ± 49	121.8 ± 62	112.3 ± 46	169.4 ± 140
$b(\times 10^3)$	2.44 ± 0.83	2.23 ± 1	5.3 ± 6.4	4.6 ± 7	$2 \times 10^{12} \pm 10^{12}$

Table 8: Comparison of results obtained with different virtual fields for Voce's model.

	Homogeneous test	Heterogeneous test			
		OVF1	VF2	VF3	VF4
	Av. $\pm$ 2 std.	Av. $\pm$ 2 std.	Av. $\pm$ 2 std.	Av. $\pm$ 2 std.	Av. $\pm$ 2 std.
σ_0(MPa)	198.1 ± 7	203.6 ± 13	195 ± 14	200 ± 20	159 ± 86
C(GPa)	30.7 ± 6	29.6 ± 3	32.2 ± 5.2	31.1 ± 9	24.6 ± 25
γ	292 ± 52	262.4 ± 60	260 ± 45	260 ± 90	139 ± 124

Table 9: Comparison of results obtained with different virtual fields for the NLKH model.

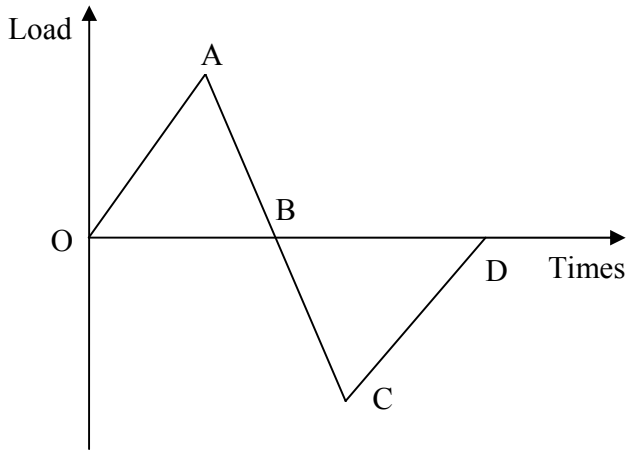

Figure 1: Diagram of loading.

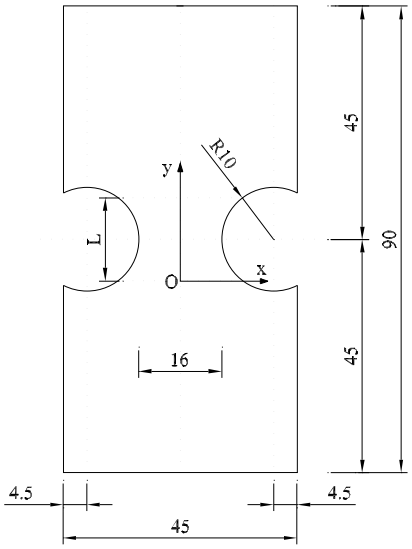

Figure 2: Geometry of the specimen (dimensions in mm).

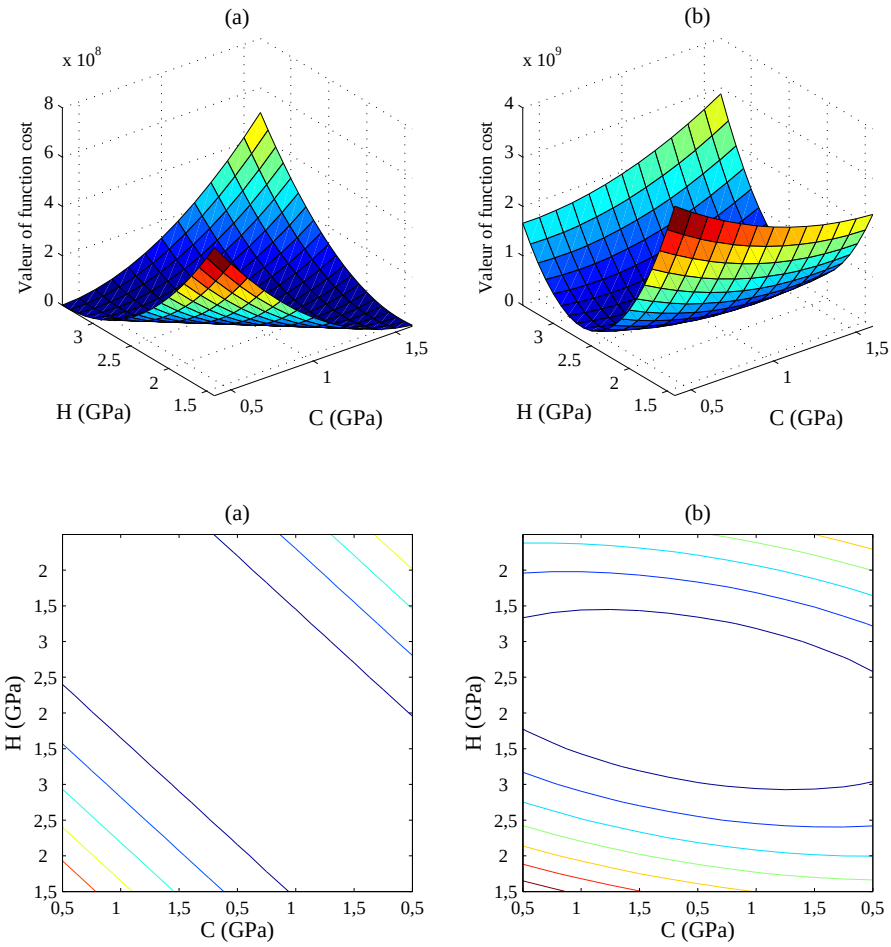

Figure 3: Plots of the cost function for load paths (a) LP1 and (b) LP4.

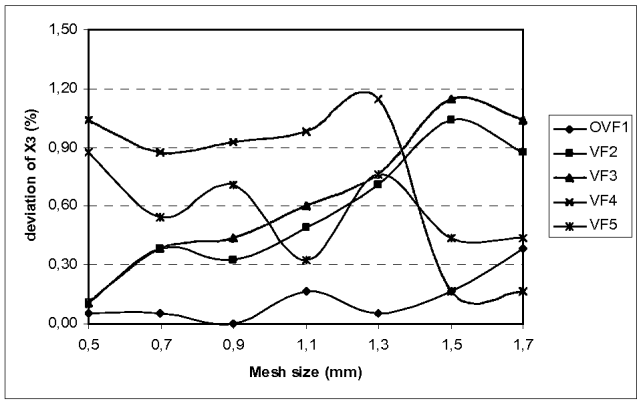

Error (in %) obtained in the identification of X_3

(a)

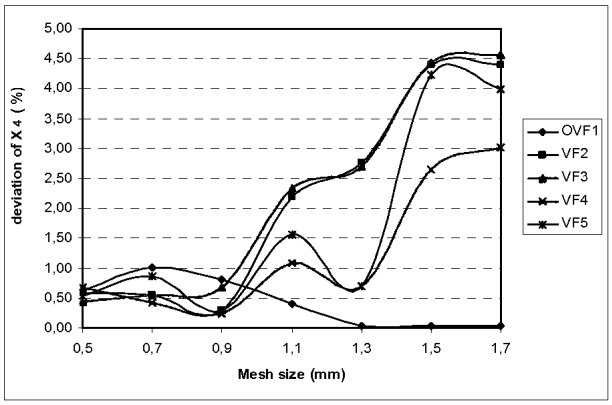

Error (in %) obtained in the identification of X_4

(b)

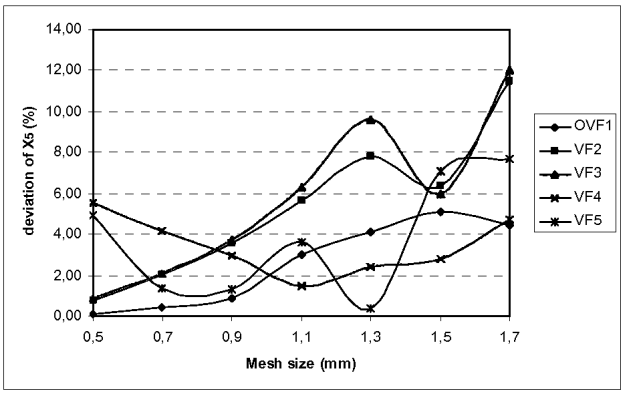

Error (in %) obtained in the identification of X_5

(c)

Figure 4: Error (in %) obtained in the identification of X_3 (a), X_4 (b) and X_5 (c) from exact data fitted with piecewise linear functions. Effect of the mesh size used for defining the basis of piecewise linear functions.

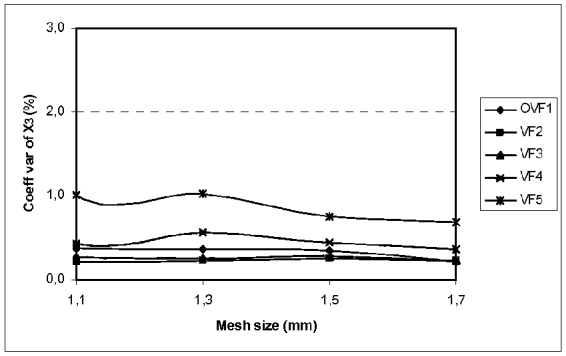

a1: Coefficient of variation of X_3 (%)

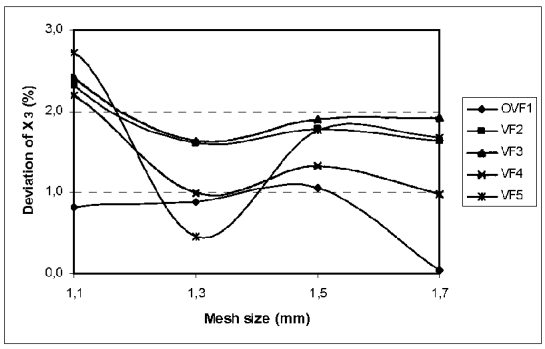

a2: Deviation of X_3 (%)

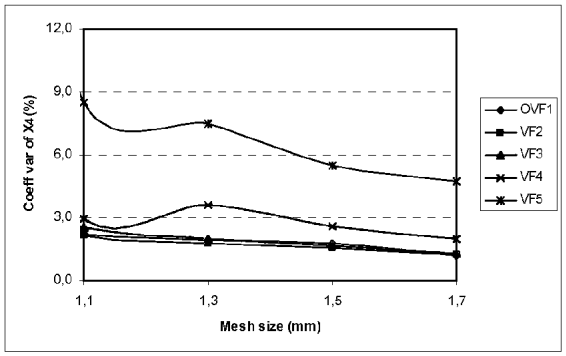

b1: Coefficient of variation of X_4 (%)

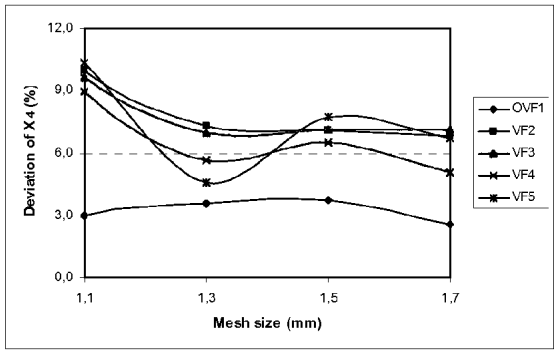

b2: Deviation of X_4 (%)

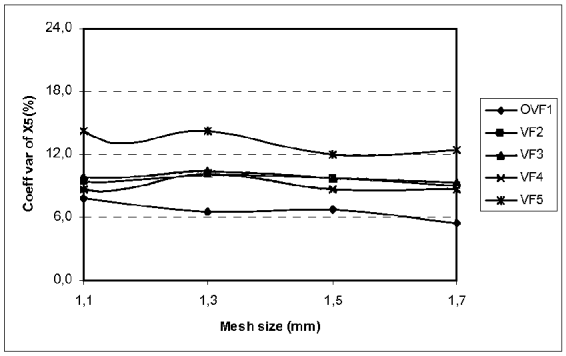

c1: Coefficient of variation of X_5 (%)

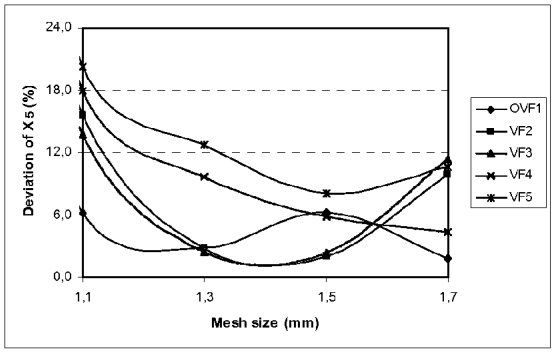

c2: deviation of X_5 (%)

Figure 5: Error (in %) obtained in the identification of X_3 (a), X_4 (b) and X_5 (c) from exact data fitted with piecewise linear functions. Noise level: γ_u=0.5 μm.

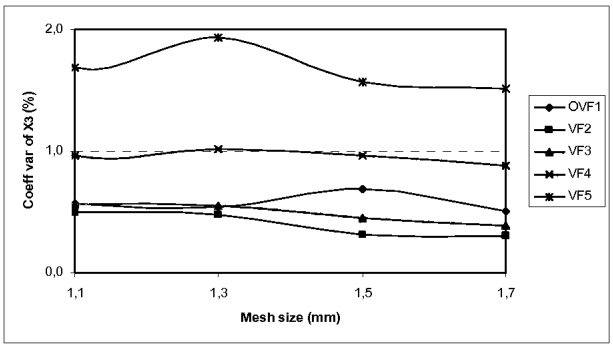

a1: Coefficient of variation of X_3 (%)

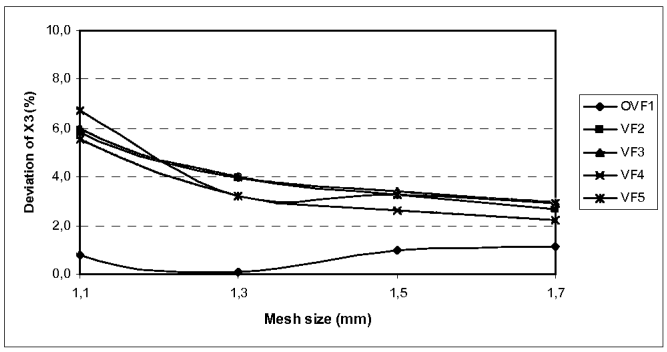

a2: Deviation of X_3 (%)

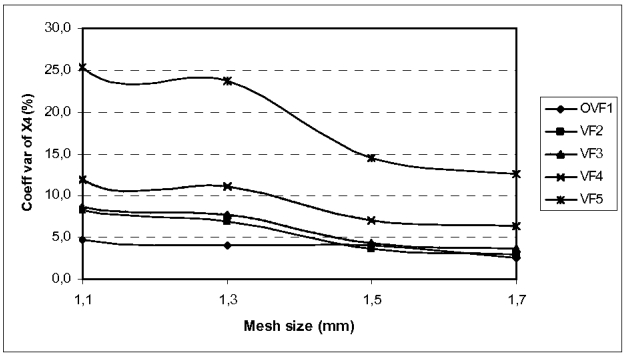

b1: Coefficient of variation of X_4 (%)

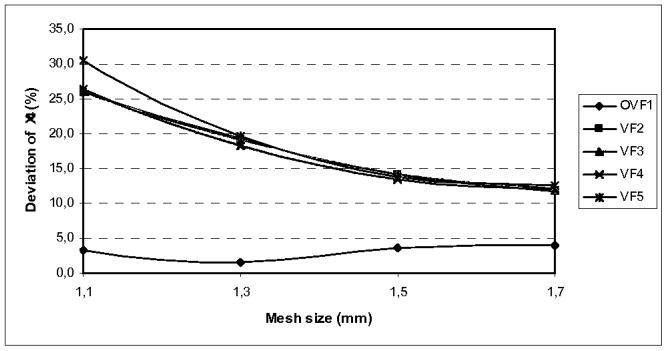

b2: Deviation of X_4 (%)

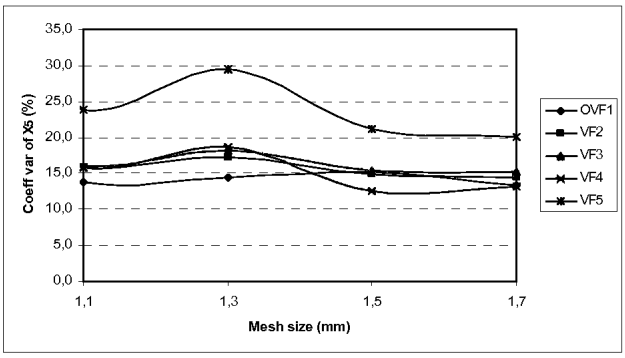

c1: Coefficient of variation of X_5 (%)

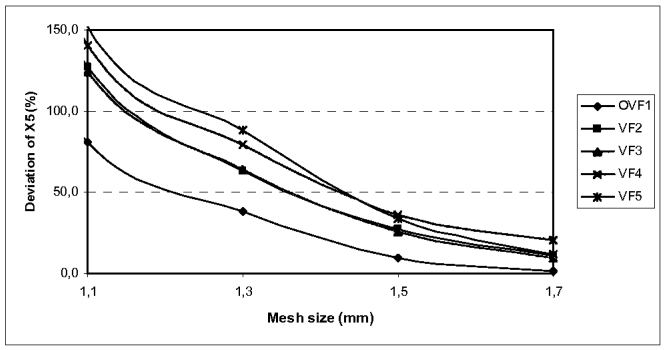

c2: deviation of X_5 (%)

Figure 6: Error (in %) obtained in the identification of X_3 (a), X_4 (b) and X_5 (c) from exact data fitted with piecewise linear functions. Noise level: γ_u=1 μm.

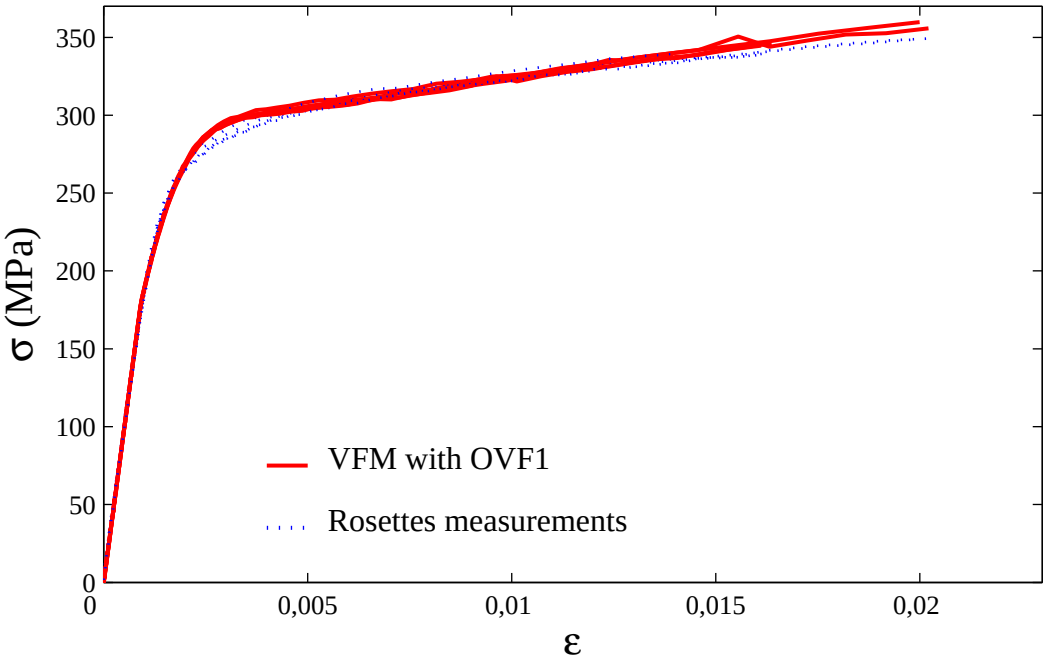

Figure 7: Stress/strain curves obtained in the first stage of the homogeneous test and comparison with the stress/strain response modeled with the Voce material parameters identified in the heterogeneous test.

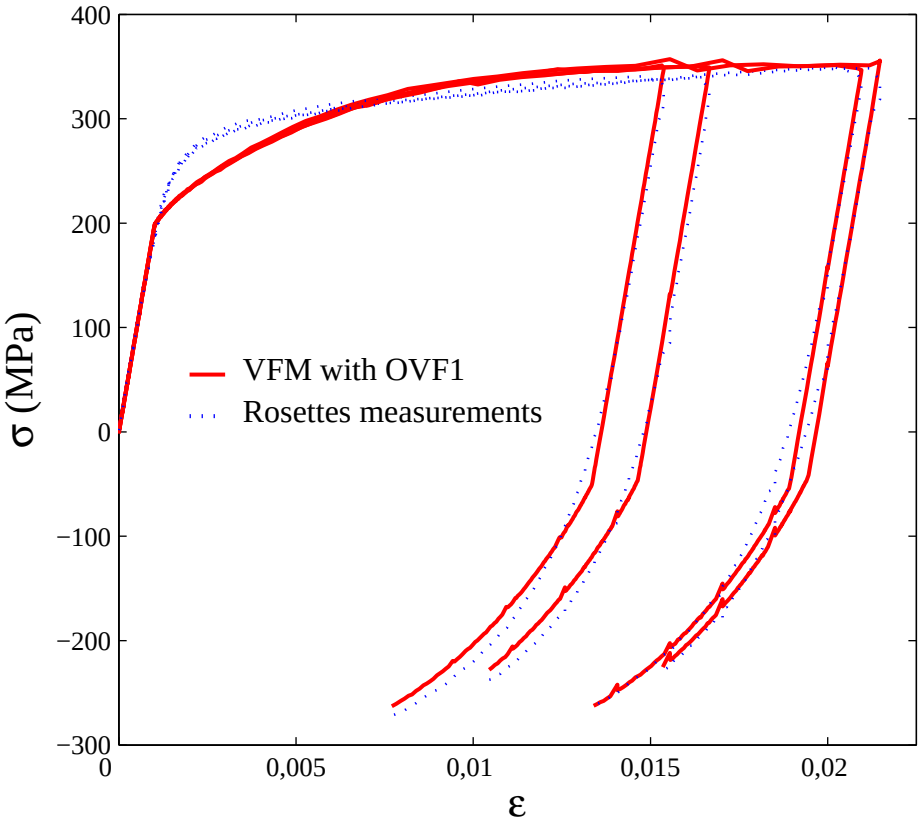

Figure 8: Stress/strain curves obtained all along the homogeneous test and comparison with the stress/strain response modeled with the NLKH material parameters identified in the heterogeneous test.

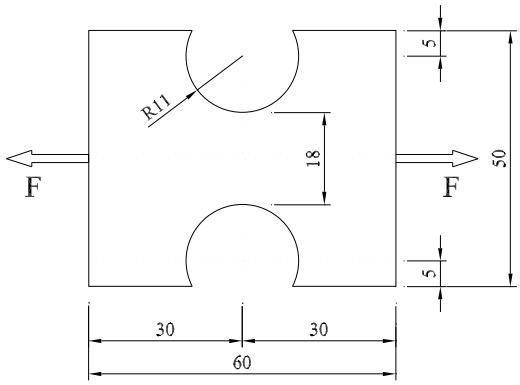

Figure 9: Geometry of the specimen (dimension in mm).

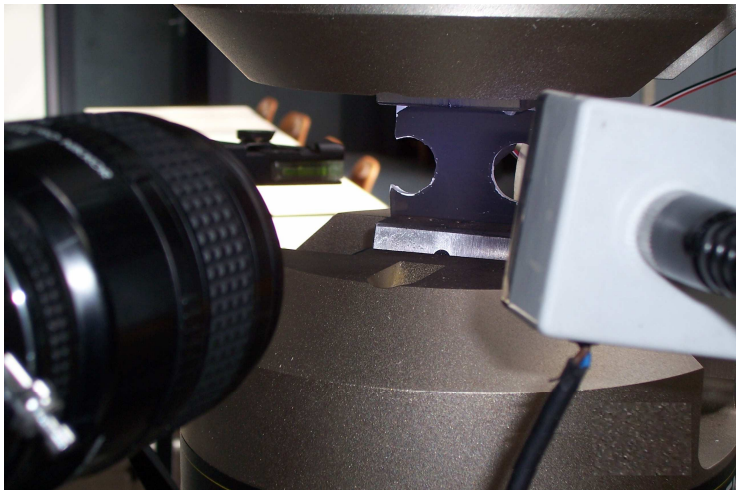

Figure 10: Picture of the specimen with the mechanical and optical set-ups.

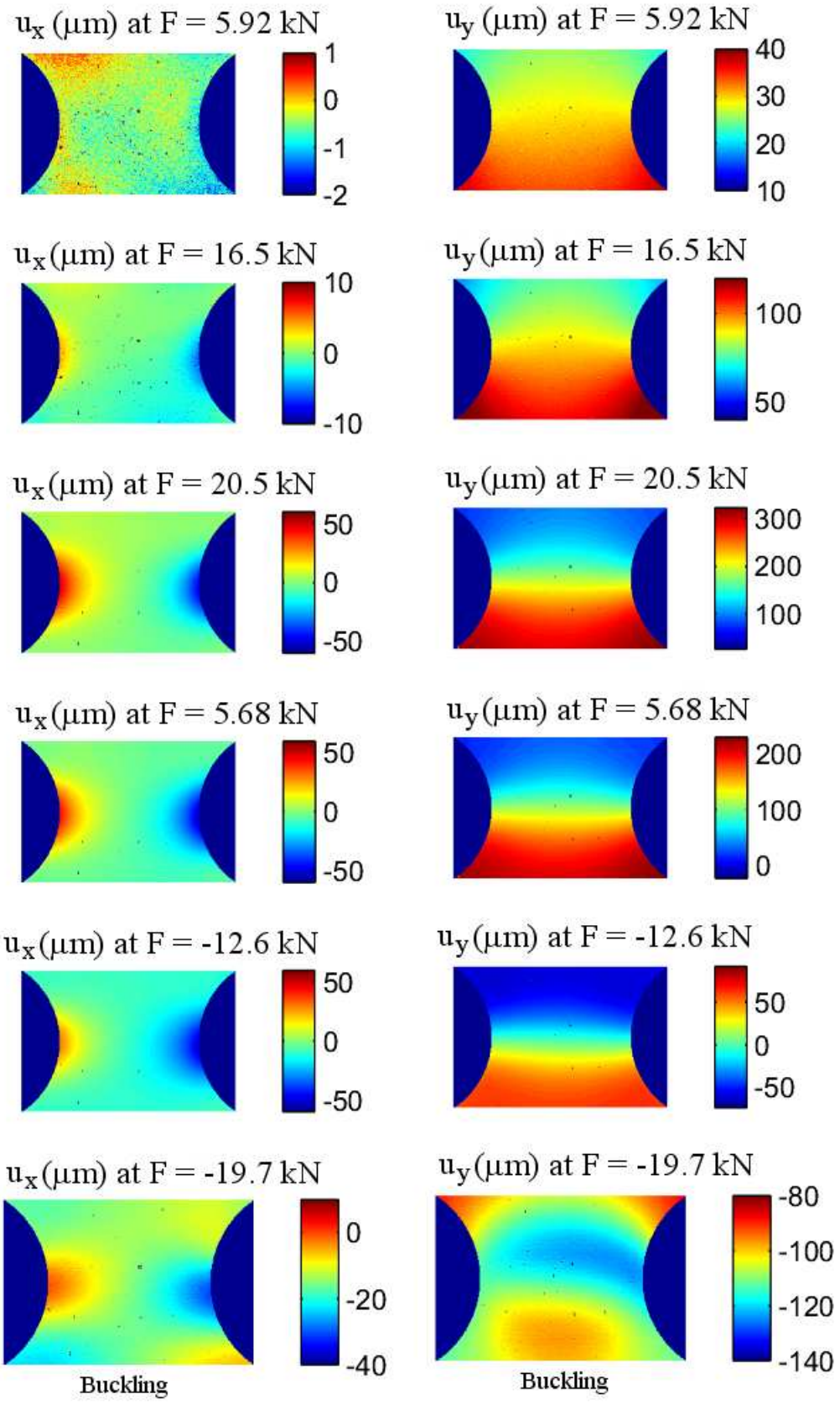

Figure 11: Displacement fields measured at different times.

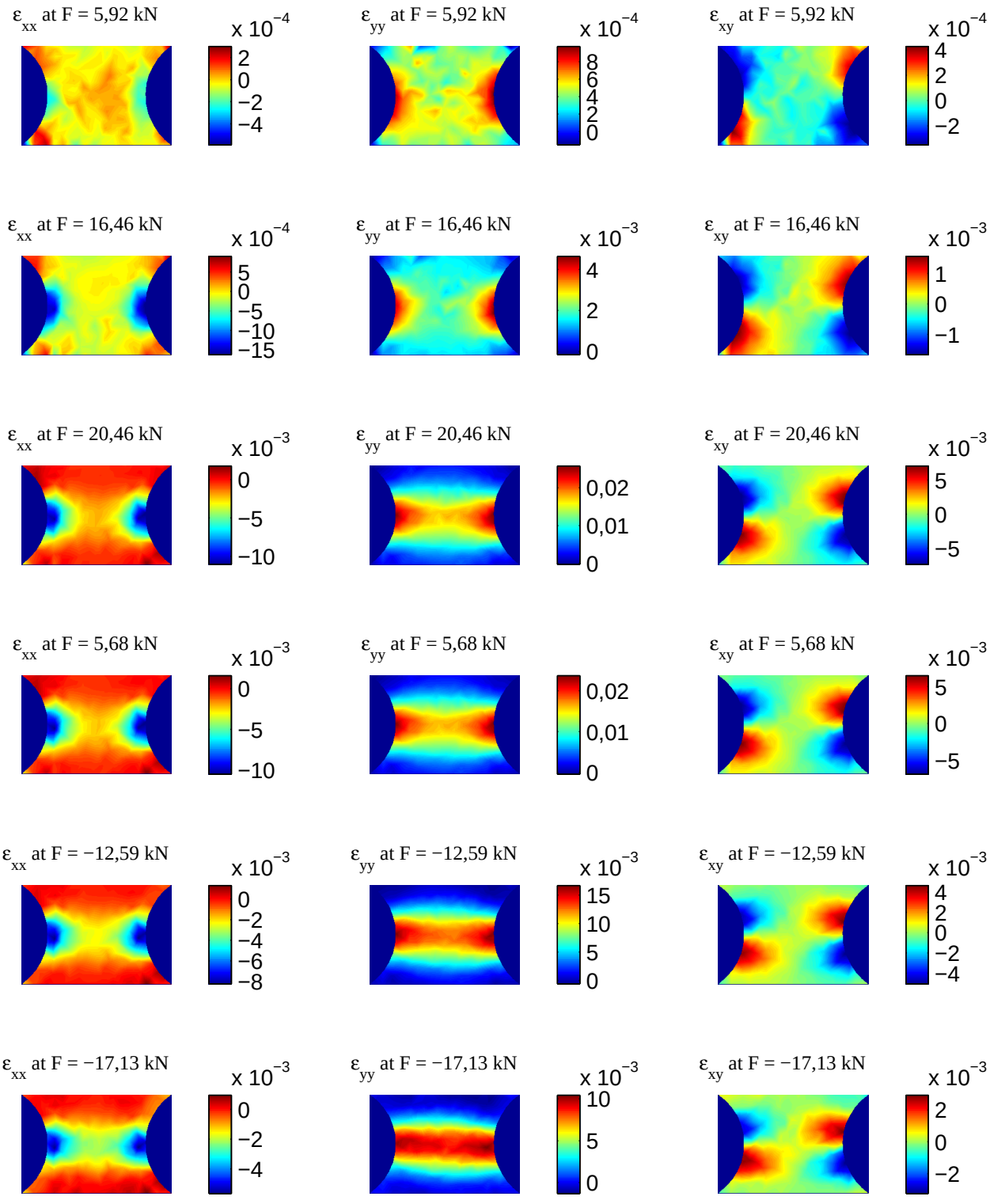

Figure 12: Continuous strain fields reconstructed from the measurements at different times.

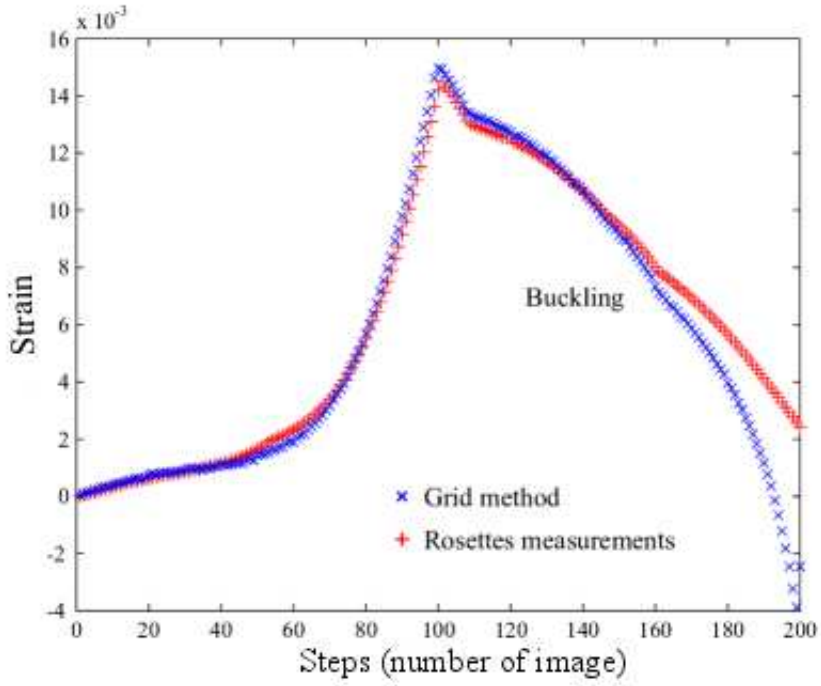

Figure 13: Comparison between strains obtained by the grid method and strain gauges.

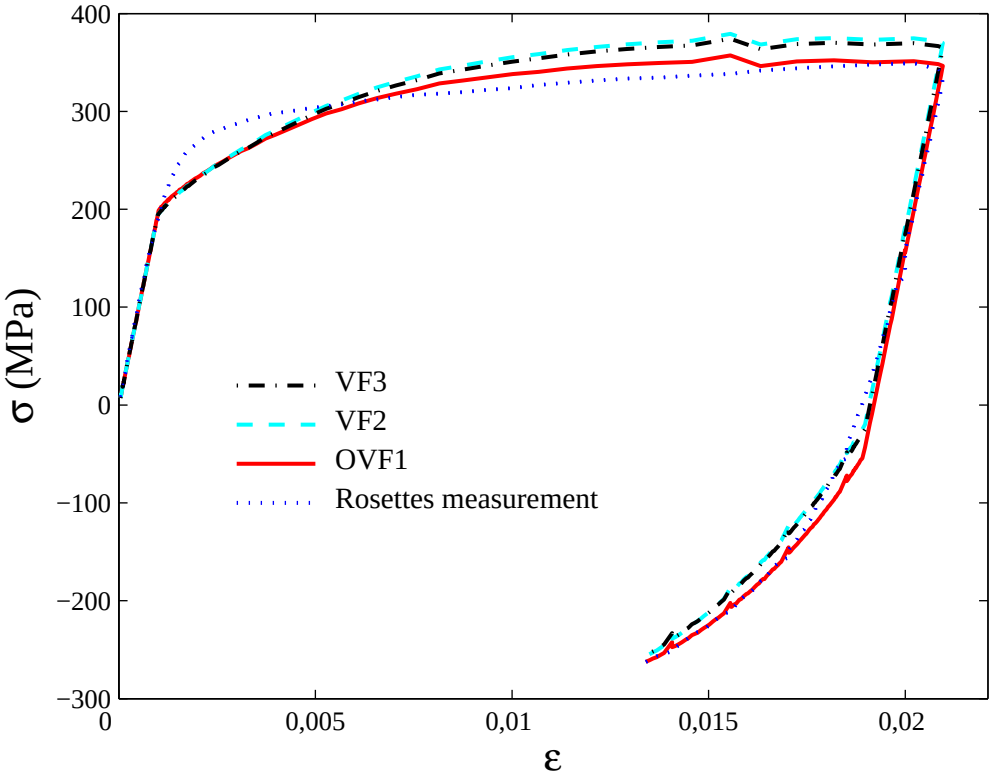

Figure 14: Superposition of the identified NLKH model with the homogeneous test (rosettes measurements) and with different virtual fields on the heterogeneous test.